Sulfate sulfur isotopes and major ion chemistry reveal that pyrite oxidation counteracts CO$_2$ drawdown from silicate weathering in the Langtang-Trisuli-Narayani River system, Nepal Himalaya

P.C. Kemeny [a,*], G.I. Lopez [a], N.F. Dalleska [a], M. Torres [b], A. Burke [c], M.P. Bhatt [d], A.J. West [e], J. Hartmann [f], J.F. Adkins [a]

[a] *Division of Geological and Planetary Sciences, California Institute of Technology, Pasadena, CA, USA*
[b] *Department of Earth, Environmental, and Planetary Sciences, Rice University, Houston, TX, USA*
[c] *School of Earth and Environmental Sciences, University of St Andrews, St Andrews, UK*
[d] *Department of Physical and Environmental Sciences, Concord University, Athens, WV, USA*
[e] *Department of Earth Sciences, University of Southern California, Los Angeles, CA, USA*
[f] *Institute for Geology, Universität Hamburg, Bundesstrasse, Hamburg, Germany*

Abstract

Drawdown of atmospheric carbon dioxide (CO$_2$) due to silicate weathering in the Himalaya has previously been implicated in Cenozoic cooling. However, over timescales shorter than that of the removal of marine sulfate (SO$_4^{2-}$), the oxidation of pyrite (FeS$_2$) in weathering systems can counteract the alkalinity flux of silicate weathering and modulate pCO$_2$. Here we present evidence from ^{34}S/^{32}S isotope ratios in dissolved SO$_4^{2-}$ (δ^{34}S$_{SO4}$), together with dissolved major ion concentrations, that reveals FeS$_2$ oxidation throughout the Langtang-Trisuli-Narayani River system of the Nepal Himalaya. River water samples were collected monthly to bimonthly throughout 2011 from 16 sites ranging from the Lirung Glacier catchment through the Narayani River floodplain. This sampling transect begins in the High Himalayan Crystalline (HHC) formation and passes through the Lesser Himalayan (LH) formation with upstream influences from the Tethyn Sedimentary Series (TSS). Average δ^{34}S$_{SO4}$ in the Lirung Glacier outlet is 3.6‰, increases downstream to 6.3‰ near the confluence with the Bhote Kosi, and finally declines to -2.6‰ in the lower elevation sites. Using new measurements of major ion concentrations, inversion shows 62–101% of river SO$_4^{2-}$ is derived from the oxidation of sulfide minerals and/or organic sulfur, with the former process likely dominant. The fraction of H$_2$SO$_4$-driven weathering is seasonally variable and lower during the monsoon season, attributable to seasonal changes in the relative influence of shallow and deep flow paths with distinct residence times. Inversion results indicate that the primary control on δ^{34}S$_{SO4}$ is lithologically variable isotope composition, with the expressed δ^{34}S value for the LH and TSS formations (median values -7.0–0.0‰ in 80% of samples) lower than that in the HHC (median values 1.7–6.2‰ in 80% of samples). Overall, our analysis indicates that FeS$_2$ oxidation counteracts much of the alkalinity flux from silicate weathering throughout the Narayani River system such that weathering along the sampled transect exerts minimal impact on pCO$_2$ over timescales >5–10 kyr and <10 Myr. Moreover, reanalysis of prior datasets suggests that our findings are applicable more widely across several of the frontal Himalayan drainages.

* Corresponding author.
   E-mail addresses: pkemeny@caltech.edu, preston.kemeny@gmail.com (P.C. Kemeny).
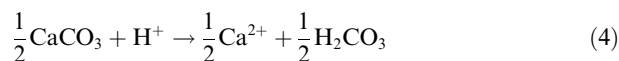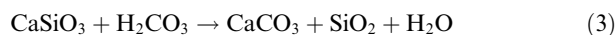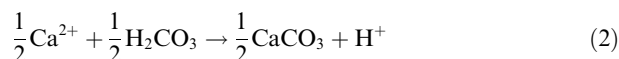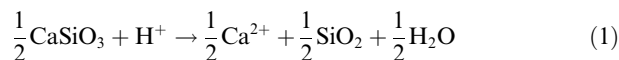
1. INTRODUCTION

Chemical weathering exerts a first-order influence on climate by regulating the flux of dissolved inorganic carbon (DIC) and alkalinity (ALK) delivered from the terrestrial surface into the ocean–atmosphere system (Walker et al., 1981; Gaillardet et al., 1999). Previously, silicate weathering of the Himalaya has been implicated in the long-term cooling of the Cenozoic (Raymo et al., 1988; Raymo and Ruddiman, 1992; Zachos et al., 2001). The associated "uplift-weathering" hypothesis has inspired extensive debate on the nature and controls of silicate weathering, both in the Himalaya and globally, with a particular emphasis on interpreting the Cenozoic rise in marine ^{87}Sr/^{86}Sr (Elderfield, 1986; Veizer, 1989; Edmond, 1992; Krishnaswami and Singh, 1998; Krishnaswami et al., 1999; Myrow et al., 2015). The controls on chemical weathering have been traditionally posed as a dichotomy between physical processes like uplift and erosion (Raymo and Ruddiman, 1992; Huh et al., 1998; Riebe et al., 2001; Millot et al., 2002) versus climate mechanisms related to temperature and the hydrologic cycle (Walker et al., 1981; White and Blum, 1995; Dessert et al., 2003). The debate has now shifted to reflect the continuum between chemical and physical controls as reflected in kinetically-limited weathering regimes and transport-limited or supply-limited weathering regimes (Stallard and Edmond, 1983; West et al., 2005; Maher and Chamberlain, 2014; Hilton and West, 2020). The Himalaya has continued to feature prominently in this discussion due to its varied lithology, topography, and potential role in Cenozoic cooling.

The role of the Himalaya in modulating Cenozoic atmospheric carbon dioxide (CO$_2$) levels remains an open question in part because the flux of silicate alkalinity from the major Himalayan rivers is relatively minor in the global context (France-Lanord and Derry, 1997; Galy and France-Lanord, 1999). This seemingly modest flux raises basic questions about whether Himalayan silicate weathering could have driven Cenozoic pCO$_2$ decline. At the same time, without compensatory feedbacks, even modest increases in silicate weathering fluxes caused by Himalayan uplift could have quickly removed all CO$_2$ from the atmosphere (Berner and Caldeira, 1997; Kerrick and Caldeira, 1999). To counteract such an over-drawdown of pCO$_2$, prior work has invoked a coincident flux of negative alkalinity through pyrite (FeS$_2$) oxidation (Torres et al., 2014), synorogenic metamorphic decarbonation (Bickle, 1996; Becker et al., 2008; Evans et al., 2008), a decrease in the magnitude of silicate weathering elsewhere (François and Walker, 1992; Kump and Arthur, 1997; Li and Elderfield, 2013), a decrease in burial of organic carbon (C$_{org}$) (Raymo, 1994), an increase in oxidation of petrogenic C$_{org}$ (Beck et al., 1995), an increase in the subduction of pelagic carbonate sediments (Caldeira, 1992), or an increase in the formation of authigenic aluminosilicate minerals (Raymo and Ruddiman, 1992). This article explores the feasibility of the first hypothesis, that of sulfide mineral oxidation (Torres et al., 2014), through measurements of the ^{34}S/^{32}S isotope ratio of dissolved sulfate (SO$_4^{2-}$) and the concentrations of dissolved major ions in river water
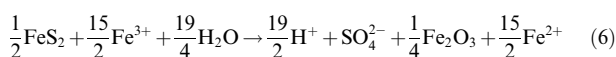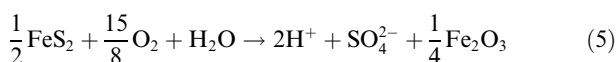
from the Langtang-Trisuli-Narayani River system in the Nepal Himalaya.

Previous research on chemical weathering of the Himalaya has focused primarily on the alkalinity flux from weathering of silicate minerals. This focus follows from the canonical framework of chemical weathering as the titration of carbonic acid (H$_2$CO$_3$) on silicate minerals (approximated as CaSiO$_3$) to generate alkalinity (Eq. (1)), which is subsequently consumed during formation and burial of marine carbonate mineral (CaCO$_3$) (Eq. (2)) (Urey, 1952). By removing one mole DIC from the ocean–atmosphere system for each mole of Ca^{2+} transferred from CaSiO$_3$ to CaCO$_3$, the chemical weathering of silicates is often described as regulating atmospheric pCO$_2$ over geologic timescales (Sundquist, 1991) (Eq. (3)). Within this same framework, the ALK and DIC sourced from weathering of carbonate minerals (Eq. (4)) are consumed during burial of marine carbonate rock. Weathering of carbonate has thus traditionally been thought to have no net impact on atmospheric pCO$_2$ over timescales longer than the 5–10 kyr timescale of marine carbonate compensation (Archer et al., 1997, 2000). Because the Nepal Himalaya is dominated by carbonate weathering (Blum et al., 1998; Galy and France-Lanord, 1999), prior studies argued that the dominant influence of Himalayan weathering on the geologic carbon cycle relates to organic carbon burial (France-Lanord and Derry, 1997; Galy et al., 2007) or metamorphic carbon fluxes (Bickle, 1996; Becker et al., 2008; Evans et al., 2008).

$$\frac{1}{2}CaSiO_3 + H^+ \rightarrow \frac{1}{2}Ca^{2+} + \frac{1}{2}SiO_2 + \frac{1}{2}H_2O \qquad (1)$$

$$\frac{1}{2}Ca^{2+} + \frac{1}{2}H_2CO_3 \rightarrow \frac{1}{2}CaCO_3 + H^+ \qquad (2)$$

$$CaSiO_3 + H_2CO_3 \rightarrow CaCO_3 + SiO_2 + H_2O \qquad (3)$$

$$\frac{1}{2}CaCO_3 + H^+ \rightarrow \frac{1}{2}Ca^{2+} + \frac{1}{2}H_2CO_3 \qquad (4)$$

The canonical weathering framework outlined above ignores sources of H$^+$ other than DIC, yet the oxidation of sulfide minerals can also provide H$^+$ that impacts the global carbon cycle (Spence and Telmer, 2005; Lerman et al., 2007; Calmels et al., 2007) (Eq. (5)). The oxidation of minerals such as FeS$_2$ generates sulfuric acid (H$_2$SO$_4$) that rapidly deprotonates to SO$_4^{2-}$, removing both ALK and dioxygen (O$_2$) from the ocean–atmosphere system. The oxidation of FeS$_2$ can also proceed through reduction of Fe^{3+} to Fe^{2+} (Eq. (6)) (Balci et al., 2007) with greater consumption of ALK per mole of released SO$_4^{2-}$. However, aerobic re-oxidization of Fe^{2+} results in the net reaction being equivalent to that of direct O$_2$ reduction (Eq. (5)). Alkalinity lost through FeS$_2$ oxidation is ultimately returned to the ocean–atmosphere system over the timescale for SO$_4^{2-}$ to be removed from the ocean in marine sediments through reduction to FeS$_2$; the residence time of SO$_4^{2-}$ in the modern ocean is approximately 10 Myr (Burke et al., 2018). The impacts of FeS$_2$ oxidation on pCO$_2$ are thus manifest during the period over which FeS$_2$-derived SO$_4^{2-}$ accumulates in seawater. Although a role for sulfide oxidation was recognized early in major

river systems (Rabinovich and Grinenko, 1979; Stallard and Edmond, 1983), including in the Himalaya (Galy and France-Lanord, 1999), FeS_2 oxidation as a globally-relevant sink of alkalinity has only recently been appreciated (Torres et al., 2014; Burke et al., 2018).

$$\frac{1}{2}FeS_2 + \frac{15}{8}O_2 + H_2O \rightarrow 2H^+ + SO_4^{2-} + \frac{1}{4}Fe_2O_3 \qquad (5)$$

$$\frac{1}{2}FeS_2 + \frac{15}{2}Fe^{3+} + \frac{19}{4}H_2O \rightarrow \frac{19}{2}H^+ + SO_4^{2-} + \frac{1}{4}Fe_2O_3 + \frac{15}{2}Fe^{2+} \quad (6)$$

More broadly, any source of SO_4^{2-} entering the ocean–atmosphere system without charge compensation by conservative cations removes ALK. For example, the oxidation of organo-sulfate moieties to SO_4^{2-} and DIC consumes 2 moles ALK per mole SO_4^{2-}, the same stoichiometry as FeS_2 oxidation (Eq. (5)). When considering the role of sulfur as a source of H^+ for weathering, what matters is thus the provision of SO_4^{2-} without the addition of conservative cations, rather than the oxidation of sulfide within any particular mineral phase. The relative importance of sulfide mineral oxidation versus the oxidation of modern or rock-bound organic sulfur (S_{org}) depends on factors such as the relative abundance of S-bearing phases, the availability of oxidants, and the presence of relevant microbial communities. However, because most S in typical siliciclastic sedimentary rocks is as sulfide minerals and not S_{org}, it is reasonable to assume that the majority of non-evaporite SO_4^{2-} liberated from rocks during weathering derives from FeS_2 oxidation. Here we thus combine all sources of SO_4^{2-} without accompanying cation release under the umbrella term of "FeS_2 oxidation" and note that this includes SO_4^{2-} sourced to the river through oxidation of reduced carbon, as well as the oxidation of additional sulfide minerals where partner cations remain in the solid phase.

Although reactions releasing SO_4^{2-} without compensating cations have similar effects on ALK, they can have different implications for DIC and thus for pCO_2; sources of SO_4^{2-} associated with S-C bonds will typically increase ocean–atmosphere DIC upon oxidation, while sources of SO_4^{2-} from inorganic minerals are unlikely to directly impact DIC. By not resolving the DIC fluxes associated with oxidation and production of organic matter, our work thus provides only a partial view of the full influence of chemical weathering on atmospheric pCO_2 (Hilton and West, 2020). Furthermore, we do not consider the nitrogen or cation fluxes associated with biomass growth and oxidation, which may counteract or reinforce the ALK dynamics of SO_4^{2-} addition to river water. Over geologic timescales, the different sources of SO_4^{2-} may also have distinct implications for pO_2. Estimates of the full balance of organic and inorganic weathering are only available for a few settings globally (Horan et al., 2019; Hilton and West, 2020), and the Nepal Himalaya is a natural choice for future research quantifying such budgets, for example, by analysis of dissolved rhenium in river water to constrain the magnitude of C_{org} oxidation (Hilton et al., 2014).

Here, we focus on quantifying the oxidation of mineral-bound sulfide and organic sulfur in the Himalaya as one of the main understudied levers on the global carbon cycle, with particular relevance for understanding Cenozoic pCO_2 decline. In their pioneering work, Galy and France-Lanord (1999) proposed that 70% of SO_4^{2-} in samples from the Narayani River system of the Nepal Himalaya derived from FeS_2 oxidation. Using measurements of DIC $^{13}C/^{12}C$ from the same study, Torres et al. (2014) proposed that sulfide oxidation in the Ganges-Brahmaputra fully counteracts the ALK flux of silicate weathering and potentially helped to sustain pCO_2 at moderate levels throughout the Cenozoic. Any increase in pCO_2 from sulfide oxidation could have offset drawdown from increases in silicate weathering, land surface reactivity, or Cenozoic C_{org} storage (France-Lanord and Derry, 1997), or accentuated increases in pCO_2 due to synorogenic decarbonation (Bickle, 1996; Becker et al., 2008). While a major role for Himalayan FeS_2 oxidation has been proposed in the work of Galy and France-Lanord (1999) and Torres et al. (2014), it has yet to be understood in detail.

Analogous to silicate weathering, FeS_2 oxidation in the Himalaya has both physical and climatic controls. Foremost, lithology controls the abundance of available sulfide minerals and thus the ability of those lithologies to generate sulfuric acid. Moreover, FeS_2 cannot be transported more than a few km through O_2-rich environments without oxidation (Johnson et al., 2014). As a corollary, sulfide oxidation is thought to almost always be supply-limited, suggesting a strong erosional control on FeS_2 oxidation and thus a gradient across geomorphic setting (Calmels et al., 2007). Oxidation of FeS_2 may also be influenced by runoff and temperature (Brantley et al., 2013), convolving H_2SO_4 into the seasonal weathering cycle, for example, if seasonal variations in hydrology control the depth of penetration of oxidizing fluids (Winnick et al., 2017). Here we present evidence for seasonal changes in the fraction of H_2SO_4-driven weathering, complementing prior evidence from throughout the Himalaya for seasonality in carbonate weathering (Tipper et al., 2006).

Sulfur isotope ratios of dissolved SO_4^{2-} ($\delta^{34}S_{SO4} = {}^{34}R_{sample}/{}^{34}R_{VCDT} - 1$, commonly reported in ‰ relative to Vienna Canyon Diablo Troilite (VCDT) and where ^{34}R is the $^{34}S/^{32}S$ ratio of SO_4^{2-}) are a useful tool for studying FeS_2 oxidation. Previously, $\delta^{34}S_{SO4}$ was measured in the Marsyandi River of the Nepal Himalaya (Turchyn et al., 2013; Hemingway et al., 2020). Because the studied region of the Marsyandi River represents only a relatively small fraction of the total Narayani River catchment, the Nepal Himalaya remains largely uncharacterized for $\delta^{34}S_{SO4}$.

In this article we report the dissolved major ion chemistry and $\delta^{34}S_{SO4}$ of seasonal river water samples from throughout the Langtang-Trisuli-Narayani River system in order to test the impacts of lithology and seasonality on FeS_2 oxidation. Using a Monte Carlo inversion model, we show that the Narayani catchment hosts FeS_2 oxidation. We find that $\delta^{34}S_{SO4}$ is principally set by lithology and identify seasonal changes in the fraction of H_2SO_4-driven weathering. Over timescales less than approximately 10 Myr, the ALK flux of sulfuric acid weathering may completely counteract the drawdown of pCO_2 due to silicate weathering in the Langtang-Trisuli-Narayani River system.
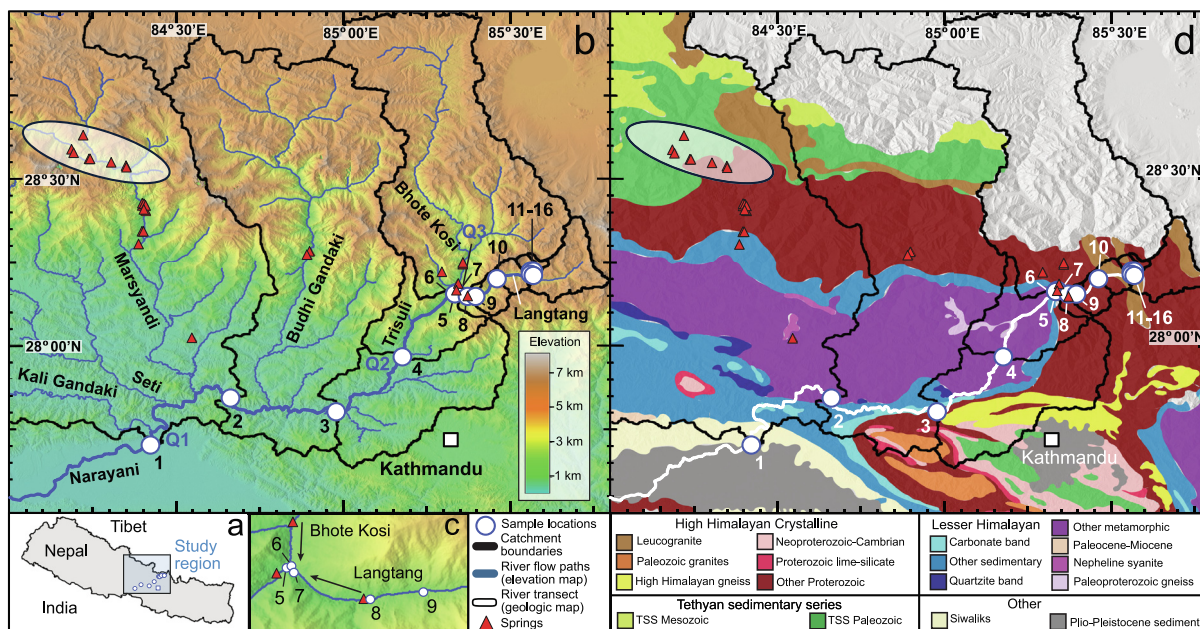
Fig. 1. Sampling locations and geologic map of the Langtang-Trisuli-Narayani River system. (a) The study region in central Nepal. (b) Elevation map with sample locations (white circles), labeled river network (blue), catchment boundaries (black), and geothermal springs (red triangles). Q1–Q3 indicate the locations of gauging stations. Shaded oval indicates approximate location of samples described in Turchyn et al. (2013) and Hemingway et al. (2020). Elevation color bar applies to (b) and (c) panels. (c) Elevation map at the confluence of the Langtang and Bhote Kosi rivers showing the relative positions of LNS-5 through LNS-9. (d) Geologic map of Nepal (Roback et al. (2018) after Dhital (2015)). Sample sites span the High Himalayan Crystalline and Lesser Himalayan sequences; although incompletely mapped, the Tethyn Sedimentary Series likely extends east into Tibet to be drained through the Bhote Kosi. Elevation data are from the Shuttle Radar Topography Mission, and locations of springs are from Evans et al. (2008) and Becker et al. (2008). (For interpretation of the references to color in this figure legend, the reader is referred to the web version of this article.)

2. METHODS

2.1. Field methods and sample context

2.1.1. Sample collection

The samples analyzed in this study are river waters from the Langtang-Trisuli-Narayani River system in central Nepal (Fig. 1), previously presented in Bhatt et al. (2018). Briefly, samples were collected monthly or bimonthly throughout 2011 at 16 sites (LNS-1 through LNS-16) ranging in elevation from 169 m to 3989 m (Fig. 1b). During collection each sample was filtered through a 0.45 μm polycarbonate filter into a single 100 mL acid-washed polyethylene bottle (Bhatt et al., 2018). Samples were not acidified, but our testing did not reveal carbonate precipitation or sorption of ions to container walls (Appendix 1). These samples are an important resource for future studies on weathering in the Nepal Himalaya because they record conditions prior to the 2015 Gorkha earthquake and associated landsliding (Roback et al., 2018).

Prior to collection, sample bottles were washed with a mixture of KOH and Neodisher LaboClean A 8 (NaOH, Na_2CO_3, $Na_2SiO_3 * 5H_2O$, $C_3Cl_2N_3NaO_3$), cleaned with 2% HCl, rinsed with water and then several times with DI water, and dried in an oven. Overall, measurements of [Cl$^-$] in our samples are higher than prior measurements from the same river system (Appendix 1, Fig. S3). Moreover, our data show coherent variations in [K$^+$]

and [Cl$^-$], which are two components of the cleaning solution. However, we do not believe that these observations reflect contamination of the samples through the cleaning protocol. The samples enriched in [Cl$^-$] also tend to be elevated in other dissolved ions, showing coherent variability across ion systems that argues against Cl$^-$ contamination. Likewise, the [Cl$^-$] and [K$^+$] variation is nearly independent of [Na$^+$], another major component of the cleaning solution, and thus not suggestive of contamination from bottle washing as a major cause of chemical variability. The results and data analyses presented below include measurements of [K$^+$], [Na$^+$], and [Cl$^-$], while calculations without [K$^+$] and [Cl$^-$] are presented as supplementary material (Appendix 4).

2.1.2. Sampling map and geologic context

The sampling transect begins in the Langtang River's headwaters in the Lirung Glacier catchment, passes through the confluence with the Bhote Kosi to join the Trisuli River at Syabru Besi, and ends in the Narayani River after crossing confluences with the Budhi Gandaki, Marsyandi River, Seti River, and Kali Gandaki (Fig. 1b). Stations LNS-16 through LNS-7 are along the Langtang River. LNS-6 is on the Bhote Kosi upstream of the confluence with the Langtang River, and LNS-5 is directly downstream of the confluence (Fig. 1c). For much of the year, the chemistry of samples from LNS-5 resembles that of LNS-6, suggesting a dominant influence from the Bhote

Kosi side of the confluence. Stations LNS-1 through LNS-4 sit on the Trisuli and Narayani Rivers and are interspersed by major tributaries. The Budhi Gandaki enters the Narayani River between LNS-3 and LNS-2, and the Marsyandi River, Seti River, and Kali Gandaki enter between LNS-2 and LNS-1. The sites are thus broadly distinguishable into three subsets based on geographic distribution: stations LNS-1 to LNS-6 along the Bhote Kosi-Trisuli-Narayani, stations LNS-7 to LNS-10 along the lower Langtang River, and stations LNS-11 to LNS-16 in the upper Langtang River as far upstream as the Lirung Glacier outlet.

The sampling transect passes through the major lithotectonic units of the Nepal Himalaya, including the High Himalayan Crystalline (HHC), the Lesser Himalayan (LH), the Siwaliks, and a portion of the floodplain (Fig. 1d). The HHC is a highly metamorphosed suite characterized by orthogneiss, paragneiss, migmatites, metapelite, and numerous leucogranite bodies (Galy and France-Lanord, 1999). The Main Central Thrust separates the HHC from the LH, and along this boundary are numerous hot springs (Bhattarai, 1980; Evans et al., 2001, 2004, 2008; Girault et al., 2014). The LH is composed of variably altered Precambrian metasediments including quartz-pelitic schist, massive dolomitic carbonates, and black shales (Pierson-Wickmann et al., 2000). The confluence of the Langtang River and the Bhote Kosi occurs at the boundary of the HHC with the LH, where hot springs are located at the town of Syabru Besi. Stations LNS-4 through LNS-2 are predominately within the LH formation, while LNS-1 sits below the Main Boundary Thrust on the floodplain built of detrital sediments.

The Tethyn Sedimentary Series (TSS) is exposed in the catchments of LNS-1 through LNS-6 and exerts a strong chemical influence on samples from these stations. The TSS is principally composed of the Phanerozoic marine shelf carbonates formed on the Indian margin prior to the collision with Eurasia, and includes black shales (Wolff-Boenisch et al., 2009). No direct observations of halite or gypsum are reported for the TSS in the Narayani catchment, although some work suggests their presence (Tshering and Bhandari, 1973 in Fort, 1996; Appendix 2). The TSS was previously found to contain FeS_2 (Bordet et al., 1971) and FeS_2 oxidation is reported in the Marsyandi River (Turchyn et al., 2013; Hemingway et al., 2020), which drains the TSS and is included in the headwaters of the catchment area captured by the most downstream sampling site in this study, LNS-1. The fraction of each catchment in our study occupied by TSS generally decreases downstream from LNS-6, although the particular fraction depends on how much unmapped area is assigned to TSS. Here we assume 90% of the unmapped region for catchments LNS-2 through LNS-6 are composed of TSS, with the other 10% occupied by HHC, and that unmapped catchment area for LNS-1 is in proportion to the mapped fractions. Notably, our observations do not depend on these fractions; rather, the critical dynamic is simply that the catchments for LNS-1 through LNS-6 contain large exposures of TSS and LH while the catchments for stations LNS-7 through LNS-16 contain much smaller exposures, if any.

2.1.3. Anthropogenic impacts on river chemistry

All samples were collected within 100 km of Kathmandu and a subset of samples were collected closer to urban centers such as Betrawati. The possibility for anthropogenic SO_4^{2-} contamination warrants particular attention given prior findings that approximately 30% of SO_4^{2-} in rivers globally is derived from pollution (Berner, 1971). Although the $\delta^{34}S$ of such pollution was previously thought to be low (Ivanov et al., 1983), recent research shows that polluted rivers can have a wide range of $\delta^{34}S_{SO4}$ values (Burke et al., 2018). We account for the indirect input of anthropogenic SO_4^{2-}, such as through atmospheric transport of pollutants and subsequent deposition, by using observations of precipitation chemistry reflecting both natural and pollutant inputs. However, our analysis does not account for any direct inputs of SO_4^{2-} to the samples. If present, such pollution would lead us to overestimate the importance of FeS_2 oxidation. Although direct inputs are unlikely in the remote upstream sites above LNS-5, the potential for direct contamination increases downstream towards the urban centers of the floodplain; if present, anthropogenic inputs are expected to be largest at stations LNS-1 through LNS-4 (Fig. 1). Such a direct SO_4^{2-} source would likely result in a progressive downstream trend in $\delta^{34}S_{SO4}$. Counter to this expectation, our data show that $\delta^{34}S_{SO4}$ changes sharply at a lithologic boundary, which argues against a dominant role for the direct input of anthropogenic SO_4^{2-}. Although there are ultimately few constraints from river pH, $[NH_4^+]$, or $[PO_4^{3-}]$ with which to evaluate direct inputs from anthropogenic activities (Collins and Jenkins, 1996), the major ion chemistry of samples leads us to suspect sources of ions from pollution are minor relative to sources from chemical weathering (Appendix 2; Fig. S6).

2.2. Experimental methods

2.2.1. Ion chromatography

The concentration of major cations and anions was measured by ion chromatography in the Environmental Analysis Center at the California Institute of Technology. The concentration of Ca^{2+}, Mg^{2+}, K^+, and Na^+ was measured on a Dionex ICS-2000 equipped with a CG12A guard column (2 mm × 50 mm) and a CS12A separator column (2 mm × 250 mm) with an isocratic 20 mM methanesulfonic eluent. SO_4^{2-} and Cl^- concentrations were measured on a Dionex ISC-3000 equipped with an AG29 guard column (2 mm × 50 mm) and an AS29 separator column (2 mm × 250 mm) with an isocratic 4.5 mM/2.5 mM Na_2CO_3/$NaHCO_3$ eluent. All major ion concentrations were measured with suppressed conductivity detection. The precision of IC measurements was typically better than 4% for samples (2σ, relative standard deviation) and always better than 11.6% (the least-reproducible ion in the least-reproducible solution, including reference solutions measured both before and after addition of HNO_3^-) but varied by element and solution (Appendix 1, Table S1). Bicarbonate (HCO_3^-) is calculated by charge balance for plotting purposes but is not included in our inversion model.

The concentration of major ions in these samples was previously measured in Hamburg and reported in Bhatt et al. (2018). During the course of this study we identified systematic differences between new measurements and the previously published values, with the discrepancy correlated to the month of sample collection (Appendix 1; Figs. S1, S2 and S3). In this analysis we use the new measurements of $[Ca^{2+}]$, $[Mg^{2+}]$, $[Na^+]$, $[K^+]$, $[Cl^-]$, and $[SO_4^{2-}]$ generated at Caltech.

2.2.2. MC-ICP-MS measurements of $\delta^{34}S_{SO4}$

River samples were evaporated to dryness overnight in acid-washed Savillex containers, dissolved in dilute hydrochloric acid, and passed through anion-exchange resin (AG 1-X8 analytical grade 100–200 mesh chloride form) to isolate SO_4^{2-}, similar to the chromatography protocols of Paris et al. (2013) and Burke et al. (2018). The isolated SO_4^{2-} was then matrix-matched to an in-house Na_2SO_4 solution previously calibrated to international reference materials and $\delta^{34}S_{SO4}$ was measured by Multi-Collector Inductively-Coupled-Plasma-Mass-Spectrometry (MC-ICP-MS) with sample-standard bracketing (Paris et al., 2013). Measurement cycles were analyzed both visually and statistically to determine outliers and a post-run correction was applied to remove instrument blank and procedural blank. The analytical method typically included two attempts to measure each eluate on a given run, and the observed differences between the two observations relative to their expected difference based on internal precision was quantified using Error-Normalized Deviation (END) (John and Adkins, 2010). After removal of samples with measurement artifacts such as rapid changes in mass biasing, the standard deviation of the internal END distribution over 10 runs ranged from 1.3 to 8.3.

The $\delta^{34}S_{SO4}$ of IAPSO seawater was measured as 20.99 $\pm$ 0.25‰ (n = 53, 2σ). The $\delta^{34}S_{SO4}$ of Switzer Falls, a local river used as an internal reference material (Burke et al., 2018), was measured as 4.25 $\pm$ 0.39‰ (n = 53, 2σ). All 121 river water samples were measured at least twice, and 48 samples were fully processed twice with a mean $\delta^{34}S$ difference of 0.20‰ between the two determinations. The reported error on each sample is taken to be the larger of either the standard deviation of blank-corrected $^{34}S/^{32}S$ ratios, or the reproducibility of references across all analytical sessions (taken to be 2σ = 0.40‰).

2.3. Principal component analysis

Variation in the concentration of Ca^{2+} is responsible for much of the absolute variance among dissolved ions. To identify trends related to the location of sampling and season of collection, we subtract the mean and divide by the standard deviation (Z-score) of the major ion chemistry and $\delta^{34}S_{SO4}$ measurements prior to performing principal component analysis (PCA) (Glover et al., 2011). Some prior work normalized dissolved ion concentrations by Na^+ prior to analysis, following an a-priori assumption of systematic changes due to seasonal dilution (Négrel et al., 1993). Here we do not further normalize the Z-scored data, meaning that any trends related to seasonal decreases in solute con-

centrations will be reflected in the results of the PCA. We plot factor loadings, which are the correlation coefficient of the Z-scored data with its projection into the basis of principal components (Négrel et al., 1993). We also plot normalized sample factor scores, which are a projection of the Z-scored data into the basis of principal components scaled by singular values and then normalized to the ratio of the maximum factor score to the maximum Euclidean distance of the plotted factor loadings.

2.4. Monte Carlo inversion model

2.4.1. Using solute chemistry to reconstruct weathering

At circumneutral pH, HCO_3^- dominates the anion budgets of many rivers and is the major reservoir of riverine DIC. As a result, the *in-situ* ALK/DIC ratio of many rivers is close to one. However, the parameter that ultimately impacts the long-term carbon cycle is the ΔALK/ΔDIC ratio of the overall weathering system sourcing ions to the river, which is different from the *in-situ* value of ALK/DIC measured in a river at any given point in space and time. Two reasons for this discrepancy are that rivers undergo gas exchange with the atmosphere (Striegl et al., 2012; Raymond et al., 2013), as well as exchange of CO_2 with the environment through aquatic respiration and photosynthesis (Quay et al., 1995). Due to this non-conservative behavior, *in-situ* $[HCO_3^-]$ reflects the integrated history of biological and physical processes within the river, in addition to chemical weathering. These processes may be important for understanding how in-river processes contribute to the global balance of photosynthesis and respiration but do not reflect the weathering processes that regulate pCO_2 on geologic timescales. Simply measuring $[HCO_3^-]$ fails to account for the upstream fluxes that have continuously modified the *in-situ* values of ALK and DIC, and thus cannot be used to calculate the ΔALK/ΔDIC ratio of the overall weathering system.

Unlike $[HCO_3^-]$, dissolved major ions are largely conservative in most river systems and can be used to reconstruct the ΔALK/ΔDIC ratio of weathering. To do so for samples from the Langtang-Trisuli-Narayani River system, the contribution of distinct lithologies to the river dissolved load was calculated using a Monte-Carlo inversion model (Négrel et al., 1993; Gaillardet et al., 1999; Torres et al., 2016; Burke et al., 2018; Hemingway et al., 2020). This inversion is analogous to prior studies of river chemistry both globally (Gaillardet et al., 1999) and in the Himalaya specifically (Bickle et al., 2015), but differs from the forward-modeling common in some prior work in the region (Galy and France-Lanord, 1999; Tipper et al., 2006). We discuss the results of our full inversion model below and include as supplementary material a subset of analogous results for a forward model (Appendix 4; Fig. S18) that uses seawater ratios for precipitation (Sarmiento and Gruber, 2006). We derive two parameters from inversion results previously introduced in Torres et al. (2016), R and Z, which respectively reflect the relative amount of silicate and carbonate weathering and the relative importance of CO_2 and H_2SO_4 as sources of H^+ for weathering reactions. Because the ΔALK/ΔDIC of the

weathering system is a simple function of the values of R and Z, our analysis focuses on their relative values as well as spatial and seasonal changes in the two parameters.

2.4.2. Inversion end-members

The inversion uses two carbonate end-members, two silicate end-members, and precipitation (Table 1). Motivating observations for our selections are given in Appendix 2, including comparison of our carbonate and silicate end-members with those used in prior work and our decision to exclude evaporite minerals and hot springs from our primary inversion; results including evaporites (Claypool et al., 1980; Valdiya, 1980; Sarin and Krishnaswami, 1984; Singh and Singh, 2010) and hot springs (Evans et al., 2004) are given in Appendix 4. Guided by observations of downstream changes in Mg^{2+}/Σ^+ (where $\Sigma^+ = Ca^{2+} + Mg^{2+} + Na^+ + K^+$ in units of charge equivalents) we separate carbonate contributions into those from calcite and dolomite. We do not include Na^+ or K^+ in the carbonate end-members; this decision is enabled by the normalization to Σ^+ rather than Na^+, which leaves the end-members free to be stoichiometric. Coherently changing K^+/Na^+ ratios motivates the use of two silicate end-members. The first end-member is called 'silicate' and is assigned a high Na^+/Σ^+ and low K^+/Σ^+, while the second end-member is called 'biotite' and is assigned Na^+/Σ^+ and K^+/Σ^+ opposite to the silicate end-member (Table 1). The silicate end-member represents generic silicate weathering (e.g., feldspars, muscovite), while the biotite end-member represents a K^+-rich phase which may be preferentially weathered during the monsoon season to increase K^+/Na^+.

Most studies in the Himalaya have appealed to the existence of an end-member with a Cl^-/Na^+ ratio near 1. Galy and France-Lanord (1999) accounted for the Cl^- in excess of precipitation inputs using a NaCl end-member, and subsequent work has often used a Cl-rich hot spring (Evans et al., 2004; Tipper et al., 2006) or seawater (Bhatt et al., 2018). The lack of evaporite minerals or high-Cl^-/Σ^+ hot springs along most of our sampling transect (Fig. S4) suggests that precipitation sources nearly 100% of Cl^- in our samples. As a result, the precipitation end-member is the only source of Cl^- in our primary inversion model. Changing this assumption impacts results for the fraction of carbonate weathering but exerts only minimal influence on the calculated fraction of H_2SO_4-driven weathering (Appendix 4). The chemical ratios of the precipitation end-member are determined from observation (Handa, 1968; Sequeira and Kelkar, 1978; Galy and France-Lanord, 1999; Bhatt et al., 2000; Shrestha et al., 2002; Hren et al., 2007; Andermann et al., 2011; Balestrini et al., 2014; Tripathee et al., 2014; Panthi et al., 2015) (Fig. S5).

Torres et al. (2016) and Burke et al. (2018) represent two different approaches to account for FeS_2 oxidation in river chemistry. In Torres et al. (2016), FeS_2 oxidation is included directly in the inversion by allowing silicate and carbonate end-members to have non-zero SO_4^{2-}/Σ^+ and well-defined $\delta^{34}S$ values. In Burke et al. (2018), FeS_2 oxidation is calculated post-inversion through SO_4^{2-} mass balance. Our analysis combines the SO_4^{2-}/Σ^+ approach of Torres et al. (2016) with the post-inversion calculation for the $\delta^{34}S$ of FeS_2 ($\delta^{34}S_{FeS2}$) allowed in the approach of Burke et al. (2018). Following Torres et al. (2016), we take the SO_4^{2-}/Σ^+ ratio of the non-precipitation end-members to reflect H_2SO_4-driven weathering. Using the measured sample $\delta^{34}S_{SO4}$ and precipitation $\delta^{34}S_{SO4}$, we then calculate by mass balance the $\delta^{34}S$ of the SO_4^{2-} sourced from the calcite, dolomite, silicate, and biotite end-members, which we take as the value of $\delta^{34}S_{FeS2}$. Each river sample thus constrains a distribution of possible $\delta^{34}S_{FeS2}$ values. Note that these inversion-constrained values of $\delta^{34}S_{FeS2}$ reflect the net $\delta^{34}S$ of SO_4^{2-} delivered without conservative cations; that is, values of $\delta^{34}S_{FeS2}$ formally reflect SO_4^{2-} sourced from both sulfide mineral oxidation and S_{org} oxidation, as opposed to the $\delta^{34}S$ of FeS_2 mineral specifically.

2.4.3. Inversion methodology

On a given iteration, the Ca^{2+}/Σ^+, Na^+/Σ^+, K^+/Σ^+, and Cl^-/Σ^+ of each end-member were pulled randomly from normal distributions with end-member-specific means and standard deviations (Table 1). The ratio SO_4^{2-}/Σ^+ was pulled from a normal distribution for the precipitation end-member, where observations inform the expected range of values. Because there is little empirical evidence for the fraction of H_2SO_4-driven weathering associated with each lithology, the SO_4^{2-}/Σ^+ for each non-precipitation end-member was pulled from a uniform distribution between 0 and 1. All distributions were truncated with a lower bound of zero, and those with a numerator constituent to Σ^+ were truncated with an upper bound of 1. The ratios of Mg^{2+}/Σ^+ for each end-member were calculated to ensure mass balance based on the other cation ratios (although indicated in Table 1, the Mg^{2+}/Σ^+ distributions were not drawn directly). If a calculated Mg^{2+}/Σ^+ was negative, the entire process was repeated up to 500 times or until a set of physically realizable, mass balanced end-members was generated. On a given iteration the river data for $[Ca^{2+}]$, $[Mg^{2+}]$, $[Na^+]$, $[K^+]$, $[Cl^-]$, and $[SO_4^{2-}]$ were altered by values pulled randomly from a normal distribution with mean

Table 1
End-member means and uncertainty (normal distributions). Precipitation is assigned a $\delta^{34}S_{SO4}$ distribution of $17\pm4‰$.

End-Member	Ca^{2+}/Σ^+	Mg^{2+}/Σ^+	Na^+/Σ^+	K^+/Σ^+	Cl^-/Σ^+	SO_4^{2-}/Σ^+
Precipitation	0.59 ± 0.20	0.13 ± 0.04	0.21 ± 0.18	0.07 ± 0.04	0.25 ± 0.23	0.17 ± 0.03
Silicate	0.15 ± 0.05	0.35 ± 0.10	0.40 ± 0.10	0.10 ± 0.10	0.00 ± 0.00	$0.00–1.00$
Biotite	0.15 ± 0.05	0.35 ± 0.10	0.10 ± 0.10	0.40 ± 0.10	0.00 ± 0.00	$0.00–1.00$
Calcite	1.00 ± 0.00	0.00 ± 0.00	0.00 ± 0.00	0.00 ± 0.00	0.00 ± 0.00	$0.00–1.00$
Dolomite	0.50 ± 0.10	0.50 ± 0.10	0.00 ± 0.00	0.00 ± 0.00	0.00 ± 0.00	$0.00–1.00$

of zero and standard deviation corresponding to analytical precision (Appendix 1).

The resulting set of river observations and end-member chemistry was solved using the MATLAB function *fmincon*; the optimization cost function was the sum of squared proportional offsets between observations and model estimate, constrained to deliver positive solutions, and used as an initial condition the solution from standard least-squares inversion. Simulation results were not accepted if any variable was more than 15% discrepant from observations, meaning that in all accepted inversion instances the sum of fractional contributions from end-members was between 85% and 115% of each observation. Up to one hundred thousand simulations were attempted; the first one thousand successful simulations for each sample were kept. All samples were successfully inverted one thousand times except the July and August samples at LNS-4 (0 successes) and the August sample at LNS-7 (233 successes). In most calculations we use the median of accepted simulation results and take the 5th and 95th percentiles of accepted simulation results as the inversion error. We note that the full 5th to 95th percentile range should be considered possible because the results of river inversions can be sensitive to the introduction of additional elemental or isotope systems (Torres et al., 2016). All inversion calculations were conducted in MATLAB through the High Performance Computing Center at Caltech.

2.4.4. Influence of secondary carbonate precipitation

Two assumptions of the Monte Carlo inversion are that the net solute release from each end-member is described by the range of chemical ratios we sample, and that these weathering products mix conservatively. However, evidence from dissolved chemistry (Jacobson et al., 2002), bedload chemistry (Bickle et al., 2015), and Ca^{2+} isotope ratios (Tipper et al., 2008) all indicate that there is secondary calcite precipitation in Himalayan rivers. Some evidence positively correlates the fraction of Ca^{2+} lost from solution with the strength of silicate weathering (Bickle et al., 2015), so that the impacts of secondary calcite formation are expected to be largest during the non-monsoon season (Tipper et al., 2006). Bickle et al. (2015) estimate the magnitude of Ca^{2+} remaining after secondary carbonate precipitation to be 5–40% in the TSS and 40–100% in the HHC.

Secondary carbonate precipitation biases the interpretation of which end-members are weathering but not which acids are responsible for weathering. The first impact of secondary calcite precipitation is to decrease observed Ca^{2+}/Σ^+, causing inversions to underestimate the true fraction of carbonate weathering (Fig. S8). Assuming 50% of Ca^{2+} was removed as secondary carbonate precipitation in our HHC-dominated samples (Bickle et al., 2015), we calculate that the effect of secondary carbonate precipitation would be to lower absolute Ca^{2+}/Σ^+ by ~10% (Fig. S8). Second, secondary carbonate precipitation will increase SO_4^{2-}/Σ^+ so that it does not reflect the fraction of gross weathering driven through sulfide oxidation. We again estimate the absolute magnitude of this effect to be ~10% (Fig. S8). Given that the importance of secondary carbonate precipitation likely varies throughout the catchment, our calcula-

tions are only approximations. However, because the formation of $CaCO_3$ produces H^+, observed Σ^+ still remains a valid metric of net H^+ consumption during weathering. That is, even in the presence of secondary carbonate precipitation, the ratio SO_4^{2-}/Σ^+ reflects net sulfuric acid weathering. In detail, the shift in the relative fraction of carbonate and silicate weathering also biases the inversion-constrained ranges of end-member SO_4^{2-}/Σ^+ (Fig. S8). Because our analysis is primarily concerned with variation in SO_4^{2-}/Σ^+, $\delta^{34}S_{SO4}$, and the seasonality of FeS_2 oxidation, our findings are largely insulated against impacts from secondary carbonate precipitation and so we do not correct our data for this process.

2.5. Construction of a synthetic hydrograph

Three gauging stations along the sampling transect (Fig. 1, Q1–Q3) record similar annual hydrographs with elevated flow during the monsoon season and reduced flow during the non-monsoon (Appendix 3, Fig. S7). Discharge at Q1 and Q3 during 2011 were similar to historical data (Fig. S7a, e). Discharge data at Q2 during 2011 were mostly similar to prior data, but with an anomalously large pulse during the monsoon (Fig. S7c). To compare weathering dynamics against seasonal discharge, we constructed a synthetic hydrograph for the entire sampling transect during 2011 by combining data from the three different gauging stations. In other words, all samples are assumed to have the same relative changes in discharge with time such that the collection date can be used as a proxy for discharge. First, we normalized by the maximum flow of each year to calculate the daily fraction of maximum annual discharge. Then, these fractional terms from the three stations were summed, normalized, and averaged by month to reach a single metric for the averged monthly fraction of maximum annual discharge (Fig. S7), and it is this derived parameter against which we compare changes in chemical weathering. We also considered a synthetic hydrograph constructed from historically averaged discharge, as opposed to only the discharge data of 2011, and found similar results (Fig. S7).

3. RESULTS

3.1. Major ion chemistry

Ternary diagrams and timeseries of major ion concentrations and elemental ratios reveal both spatial and seasonal patterns (Figs. 2 and 3). The ion Ca^{2+} is the dominant cation throughout the Langtang-Trisuli-Narayani River system and accounts for 46–79% of the sum of Ca^{2+}, Mg^{2+}, Na^+, and K^+, in units of charge equivalents, except for one sample at 25% (Fig. 2a). The cation Mg^{2+} is of secondary importance and accounts for 8–32% of Σ^+. With the exception that both Na^+ and K^+ have a single outlier sample at 37%, Na^+ accounts for 5–22% of Σ^+ and K^+ accounts for 2–22% of Σ^+. Overall, the major ion chemistry of the samples is consistent with prior observations from this region (Harris et al., 1998; Galy and France-Lanord, 1999; Bhatt et al., 2009; Appendix 1). As
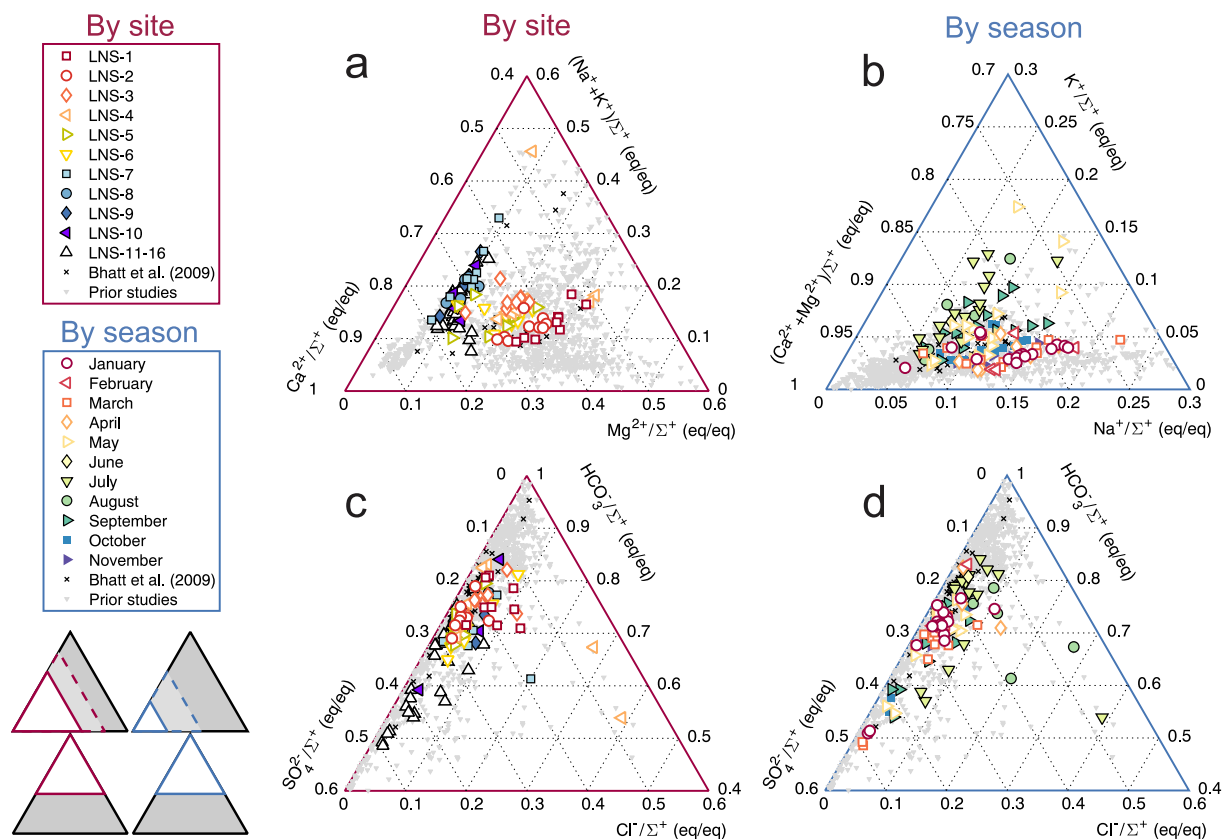
Fig. 2. Ternary diagrams for river water samples from the Langtang-Trisuli-Narayani River system show spatial and temporal patterns. Panels are color coded by either station number (a, c) or month of collection (b, d), and are subsets of the full parameter space as indicated in the schematics (lower-left: filled white triangles are plotted areas, dashed triangles contain the full dataset, and grey triangles represent the full space). (a) The dominant cation in solution is Ca^{2+}. The cation Mg^{2+} is second in relative abundance, and $Na^{+}+K^{+}$ represents a limited fraction of the charge budget. Spatial transitions between $(Na^{+}+K^{+})/\Sigma^{+}$ and Mg^{2+}/Σ^{+} indicate the differing abundance of silicate and carbonate minerals in the HHC and LH. (b) The ratios Na^{+}/Σ^{+} and K^{+}/Σ^{+} shift seasonally in relative importance, with higher K^{+}/Na^{+} ratio during the monsoon and lower ratio during the non-monsoon season. (c) The major anion in solution is HCO_3^{-}, except near the Lirung Glacier catchment where SO_4^{2-} occasionally has subequal contribution. (d) Monsoon season samples are occasionally enriched in Cl^{-}/Σ^{+} relative to samples from the non-monsoon season. Plotted values reflect raw measurements without correction for inputs from precipitation. All samples from this study are plotted in (c) and (d). One sample with $(Na^{+}+K^{+})/\Sigma^{+}$ ~60% is out of the plotting range in (a), and three samples are out of the plotting range in (b). Data from prior studies (grey triangles) are river water samples reported in Sarin et al. (1989), Galy and France-Lanord, 1999, English et al. (2000), Bhatt et al. (2000), Dalai et al. (2002), Quade et al. (2003), Evans et al. (2004), Bickle et al. (2005; 2018), Tipper et al. (2006), Wolff-Boenisch et al., 2009, Turchyn et al. (2013), and Pant et al. (2018).

found previously, samples from the Bhote Kosi and Trisuli Rivers are slightly enriched in Na^{+} and K^{+} relative to Ca^{2+} and Mg^{2+} when compared to samples from the greater Narayani River system (Evans et al., 2004).

In the high-elevation sites, values of $(Na^{+}+K^{+})/\Sigma^{+}$ and Ca^{2+}/Σ^{+} fall along a line of constant Mg^{2+}/Σ^{+} near 10% (Fig. 2a). Conversely, differences among the lower-elevation stations LNS-1 to LNS-6 are predominantly between Ca^{2+}/Σ^{+} and Mg^{2+}/Σ^{+} with muted differences in $(Na^{+}+K^{+})/\Sigma^{+}$ around 10–20%. These observations are consistent with the high elevation sites weathering the Na^{+}-rich and K^{+}-rich HHC gneiss and schist, while lower elevation sites within the LH are dominated by calcite and dolomite weathering. While the aggregate changes in $(Na^{+}+K^{+})/\Sigma^{+}$ are related to the site of sample collection, Na^{+}/Σ^{+} and K^{+}/Σ^{+} also exhibit strong trends related to the month of sample collection (Fig. 2b). At a given value

of $(Ca^{2+}+Mg^{2+})/\Sigma^{+}$, monsoon samples show a rotation to higher K^{+}/Σ^{+} and lower Na^{+}/Σ^{+} relative to samples from the non-monsoon.

The ratios Ca^{2+}/Na^{+} and Ca^{2+}/Mg^{2+} are elevated at most stations during the monsoon season (Fig. 3a, b). At LNS-4, however, both ratios are highly variable. Because $[K^{+}]$ does not coherently decline during the monsoon season and $[Na^{+}]$ does decline during the monsoon, K^{+}/Na^{+} is highest during the monsoon season at all stations. Likewise, monsoon K^{+}/Σ^{+} is elevated at all stations (Fig. 3d). Thus, while Ca^{2+}/Na^{+} is highest during the monsoon, the increase of $[K^{+}]$ relative to $[Na^{+}]$ and decline in absolute $[Ca^{2+}]$ and $[Mg^{2+}]$ results in muted seasonal change in Ca^{2+}/Σ^{+}, although with Ca^{2+}/Σ^{+} still generally higher during the monsoon season (Fig. 3c). Like $[K^{+}]$, $[Cl^{-}]$ is not always lower during the monsoon; the ratio Cl^{-}/Na^{+} is highest during the monsoon, and Cl^{-}/Σ^{+} is weakly elevated
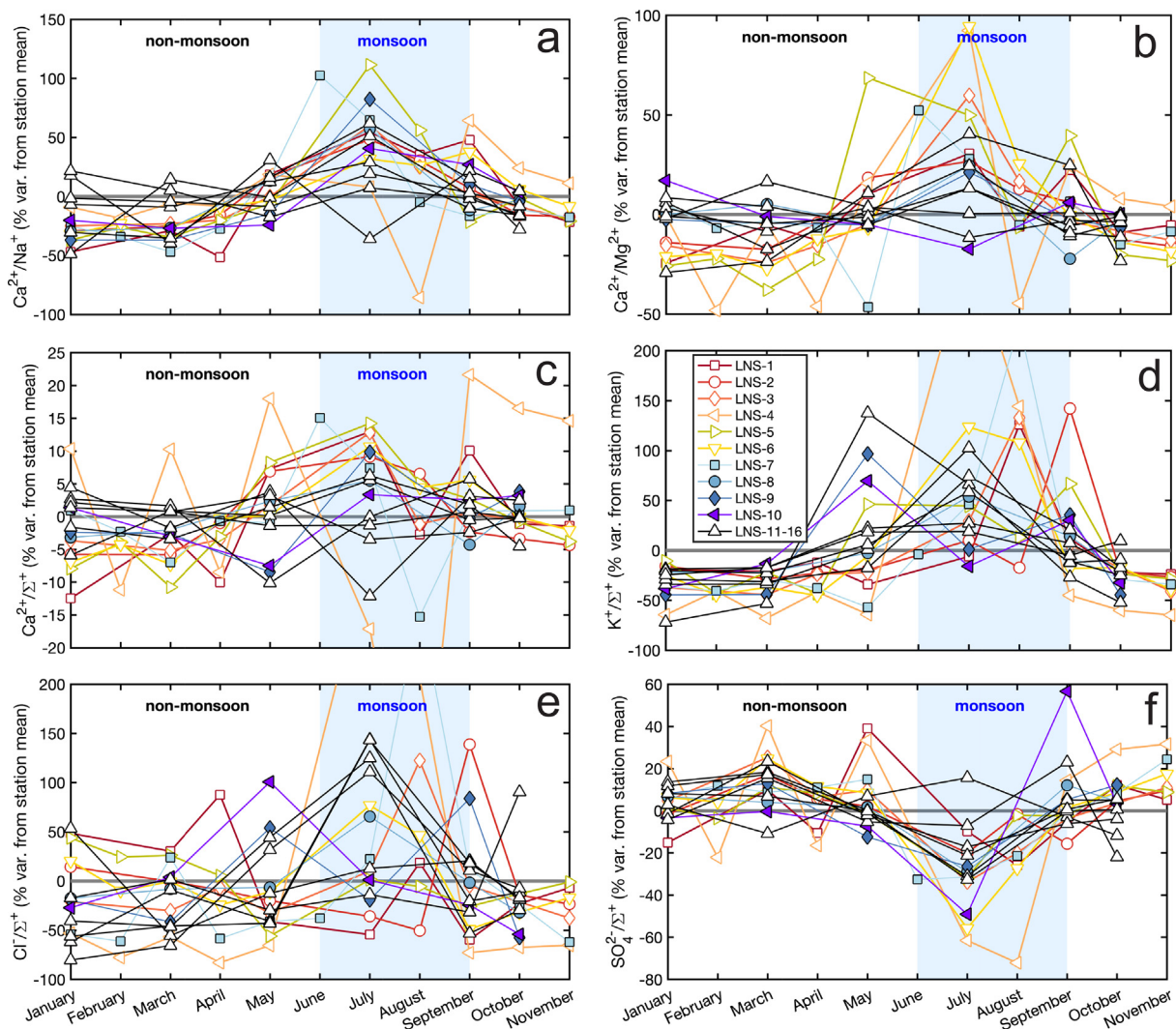
Fig. 3. Timeseries of dissolved ratios reported as the % variations from annual station means. (a) The cation ratio Ca^{2+}/Na^+ increases during the monsoon season relative to the non-monsoon. (b) The ratio Ca^{2+}/Mg^{2+} also increases during the monsoon, consistent with a shift in either the relative fraction of silicate and carbonate weathering or a shift from dolomite to calcite weathering. (c) The ratio Ca^{2+}/Σ^+ tends to increase weakly during the monsoon. (d) The ratio K^+/Σ^+ increases strongly during the monsoon. (e) The ratio Cl^-/Σ^+ shows a weak increase during the monsoon, which partially offsets the observed monsoon rise in Ca^{2+}/Σ^+ due to the high Ca^{2+}/Cl^- of precipitation (Table 1). (f) The ratio SO_4^{2-}/Σ^+ declines during the monsoon, suggesting a seasonal reduction in the fraction of weathering driven by sulfide oxidation. Note that each panel has a variable y-axis range, and that blue shading indicates the monsoon season. (For interpretation of the references to color in this figure legend, the reader is referred to the web version of this article.)

during the monsoon at most sites (Fig. 3e). While Ca^{2+}/Σ^+ is elevated during the monsoon relative to the non-monsoon, some of this increase is associated with the weak increase in Cl^-/Σ^+. That is, because Cl^-/Σ^+ increases during the monsoon, the relative supply of Ca^{2+} from precipitation also increases during the monsoon and partly decreases the Ca^{2+} attributed to lithologic weathering. Coupled with the monsoon increase in the K^+/Na^+ ratio, these observations qualitatively suggest that we only weakly recover the monsoon increase in carbonate weathering fraction previously found in some datasets from Nepal (Tipper et al., 2006) and the Ganga-Brahmaputra basin (Sarin et al., 1989).

The dissolved anion budget in all of our samples is dominated by HCO_3^-, which comprises 49–84% of Σ^+ (the sum of conservative cations is equal to the sum of anions here because HCO_3^- is solved by charge balance) (Fig. 2c). The anion SO_4^{2-} typically represents 5–30% of the budget but rises as high as 49% in a subset of samples from the headwaters at the Lirung Glacier. The anion Cl^- is typically 1–13% of the anion budget but reaches 20–39% for the July and August sampling of LNS-4 and the August sampling of LNS-7 (Fig. 2d). Notably, these three samples are those where the inversion model either found only few solutions or was unable to find any solutions. The ratio of SO_4^{2-}/Σ^+ decreases at almost all stations during the monsoon season,

with the lowest ratios found in July and August (Fig. 3f). These raw data suggest seasonality in the fraction of weathering driven by FeS$_2$ oxidation.

3.2. Spatial and seasonal variability of δ^{34}S$_{SO4}$

Values of δ^{34}S$_{SO4}$ range from −4.5‰ to 9.0‰ (Fig. 4a). Averaged annually, δ^{34}S$_{SO4}$ is 3.9‰ at station LNS-16 and increases to 6.0–6.8‰ moving downstream along the Langtang River through LNS-9, LNS-8, and LNS-7. Conversely, LNS-6 on the Bhote Kosi has an average δ^{34}S$_{SO4}$ of −2.0‰. Station LNS-5, which is after the confluence of these two river systems, has an intermediate δ^{34}S$_{SO4}$

value of 0.0‰. The value of δ^{34}S$_{SO4}$ increases within the Trisuli River to reach 0.8–2.3‰ at stations LNS-4 and LNS-3, declines to −3.7‰ at LNS-2, and finally increases to −1.5‰ at LNS-1 (Fig. 4a). Overall, the range of measured δ^{34}S$_{SO4}$ is largely consistent with prior values from the Himalaya including from the Alakananda-Bhagirathi rivers (Chakrapani and Veizer, 2006) and the Indus River Basin (Karim and Veizer, 2000).

The most notable trend in δ^{34}S$_{SO4}$ is that samples from stations LNS-1 through LNS-6 (the downstream and Bhote Kosi stations) tend to be ^{34}S-depleted relative to samples from stations LNS-7 through LNS-16 (the upstream stations) (Fig. 4b). Annual variability in δ^{34}S$_{SO4}$
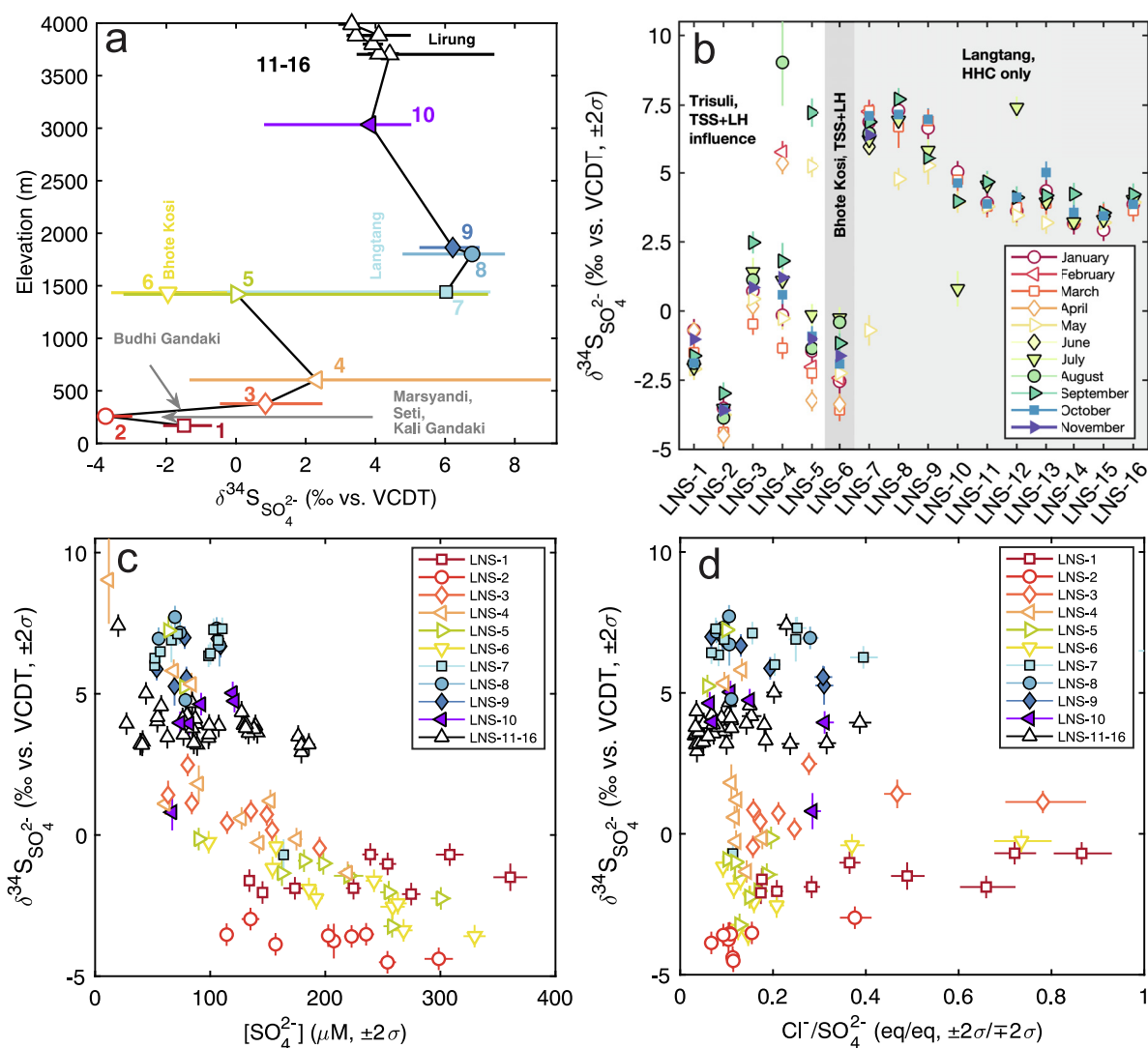

Fig. 4. River water δ^{34}S$_{SO4}$, [SO$_4^{2-}$], and Cl$^-$/SO$_4^{2-}$ coded by either (a, c, d) station number or (b) month of collection. (a) Mean station δ^{34}S$_{SO4}$ and annual range. Grey lines indicate confluences with major Narayani River tributaries. The catchments of stations LNS-7 through LNS-16 contain only HHC, while those of LNS-1 through LNS-6 contain TSS and LH as well. (b) Values of δ^{34}S$_{SO4}$ are typically higher at sites LNS-7 through LNS-16 than at sites LNS-1 through LNS-6. Values of δ^{34}S$_{SO4}$ are relatively constant throughout the year at a given station. (c) Values of δ^{34}S$_{SO4}$ against [SO$_4^{2-}$]. Across the sample suite, δ^{34}S$_{SO4}$ decreases downstream with increasing [SO$_4^{2-}$], although this relationship only seems to hold specifically for stations LNS-3 through LNS-6. (d) Values of δ^{34}S$_{SO4}$ against Cl$^-$/SO$_4^{2-}$. The lack of clear relationship argues against two-end member mixing as an explanation for the relation between δ^{34}S$_{SO4}$ and [SO$_4^{2-}$].

at a given site is muted relative to this larger spatial pattern. Stations LNS-4 and LNS-5 have the largest seasonal $\delta^{34}S_{SO4}$ variability; this is consistent with their position directly downstream of the confluence of the Bhote Kosi and Langtang Rivers, as the relative contribution of SO_4^{2-} from each upstream river likely varies seasonally. Additionally, variability in LNS-4 may be partially attributable to pollution from the urban center of Betrawati (Appendix 2).

Values of $\delta^{34}S_{SO4}$ are negatively correlated with $[SO_4^{2-}]$ when viewed across the whole dataset (Fig. 4c). At sites LNS-3 through LNS-6, $\delta^{34}S_{SO4}$ decreases seasonally with increasing $[SO_4^{2-}]$. For example, the May and September samples of LNS-5 with low $[SO_4^{2-}]$ have higher $\delta^{34}S_{SO4}$ values than samples with higher $[SO_4^{2-}]$. The non-linear decrease in $\delta^{34}S_{SO4}$ with increasing $[SO_4^{2-}]$, at the scale of either individual stations of the entire data suite, ostensibly resembles a mixing curve with multiple ‰ of scatter in $\delta^{34}S_{SO4}$ at a given value of $[SO_4^{2-}]$. However, $\delta^{34}S_{SO4}$ values are not clearly related to changes in Cl^-/SO_4^{2-} (Fig. 4d) or other major ion ratios (Fig. S9). For example, while samples from LNS-5 have a wide range of $\delta^{34}S_{SO4}$ values inversely related with $[SO_4^{2-}]$, they have only a narrow range of Cl^-/SO_4^{2-} ratios (Fig. 4d). Likewise, the set of $\delta^{34}S_{SO4}$ measurements from LNS-1 through LNS-6, although systematically lower than the set from LNS-7 through LNS-16, is not distinct in Cl^-/SO_4^{2-} (Fig. 4d). Values of $\delta^{34}S_{SO4}$ at stations LNS-1, LNS-2, and LNS-7 through LNS-10 are largely invariant, with seasonal shifts towards higher $[SO_4^{2-}]$ during the non-monsoon season (Fig. 4c), and have little relationship with Cl^-/SO_4^{2-} (Fig. 4d). The major ion chemistry of our samples thus precludes two-component mixing as an explanation for the trend of $\delta^{34}S_{SO4}$ with $[SO_4^{2-}]$; as

described below, the observations require multiple lithologic end-members with variable $\delta^{34}S$.

3.3. Principal component analysis

The PCA of Z-scored $[Ca^{2+}]$, $[Mg^{2+}]$, $[Na^+]$, $[K^+]$, $[Cl^-]$, $[SO_4^{2-}]$, and $\delta^{34}S_{SO4}$ identifies that 3 components explain 95.1% of normalized variance. The first component (PC-1) explains 66.3% of variance and relates changes among all dissolved ion concentrations with opposite changes in $\delta^{34}S_{SO4}$ (Fig. 5a). PC-1 predominantly distinguishes samples by the site of collection, not by the season of collection (Fig. 5b), and thus indicates that lithology is the first-order control on dissolved ion chemistry (as found in other settings; e.g., Bluth and Kump, 1994). PC-1 also shows seasonal influences; at a given site, factor scores of PC-1 are generally higher in samples collected during the monsoon period and lower in samples collected in the non-monsoon (Fig. 5b). The second principal component (PC-2) explains 21.0% of the normalized variance and also shows both spatial and seasonal trends (Fig. 5c). These results indicate that seasonality exerts a secondary control on major ion chemistry along the Langtang-Trisuli-Narayani River system (Bhatt et al., 2018). Using cluster analysis, Pant et al. (2018) likewise showed that in river waters from the Narayani basin, lithology exerts the dominant control on dissolved chemistry and seasonality exerts a secondary influence.

PC-2 also inversely relates $\delta^{34}S_{SO4}$ with $[SO_4^{2-}]$. Unlike PC-1, PC-2 does not strongly relate changes in $\delta^{34}S_{SO4}$ with changes in $[Ca^{2+}]$, $[Mg^{2+}]$, or $[Na^+]$, which are the major products of chemical weathering. This result indicates a mode of variability between $[SO_4^{2-}]$ and $\delta^{34}S_{SO4}$ largely independent from shifts in weathering lithology. One qualitative explana-
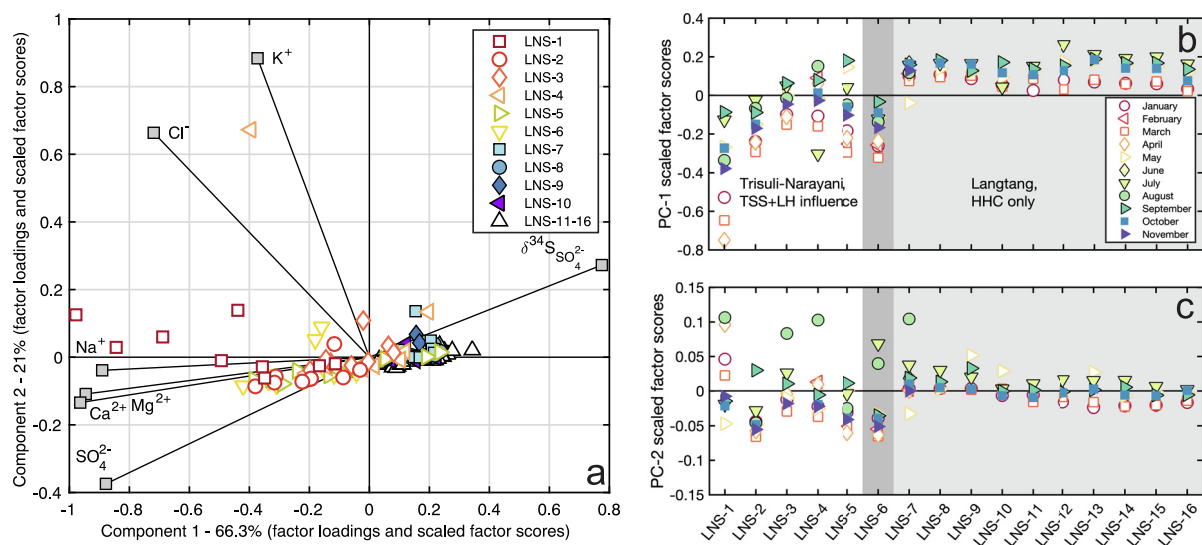

Fig. 5. (a) Biplot of principal component 1 (PC-1) and principal component 2 (PC-2). Labeled vectors indicate factor loadings, and symbols show the normalized factor scores of samples (Glover et al., 2011). Principal component 1 inversely relates $\delta^{34}S_{SO4}$ with the concentration of all cations and anions. Principal component 2 inversely relates $[SO_4^{2-}]$ and $\delta^{34}S_{SO4}$, and positively relates K^+ and Cl^-. (b) Sample factor scores of the first component, which captures the primary axis of variability in our chemical observations, principally vary by sampling site with a secondary seasonal influence. (c) Sample factor scores of the second component reflect seasonal variability, with larger seasonal changes in the Trisuli and Narayani Rivers than in the Langtang River.

tion for this observation is a shift in the $\delta^{34}S$ and weatherability of an end-member providing SO_4^{2-} to solution. An alternative explanation is microbial sulfate reduction in either the river sediments or tributaries, which would remove SO_4^{2-} and increase $\delta^{34}S_{SO4}$ (Turchyn et al., 2013).

The strongest relation in PC-2 is a positive correlation between [K$^+$] and [Cl$^-$]. Monsoon samples from the Lirung Glacier outlet show systematically higher factor scores for PC-2 than samples from the non-monsoon (Fig. 5c). Given that these samples are relatively distant from direct anthropogenic influences, the covariation of [K$^+$] and [Cl$^-$] may reflect a true weathering dynamic.

4. DISCUSSION

4.1. Mixing relations require source of ^{34}S-depleted SO_4^{2-}

The high Ca^{2+}/Σ^+ and low Na^+/Σ^+ ratios of samples from throughout the Langtang-Trisuli-Narayani River system indicate that the majority of positive charge in solution derives from either the carbonate mineral or precipitation end-members (Fig. 6a). The contribution of precipitation to the dissolved ion budgets is ultimately limited by the relative abundance of Cl$^-$ (Fig. 6b). Given that the majority of cation charge must be derived from weathering of calcite
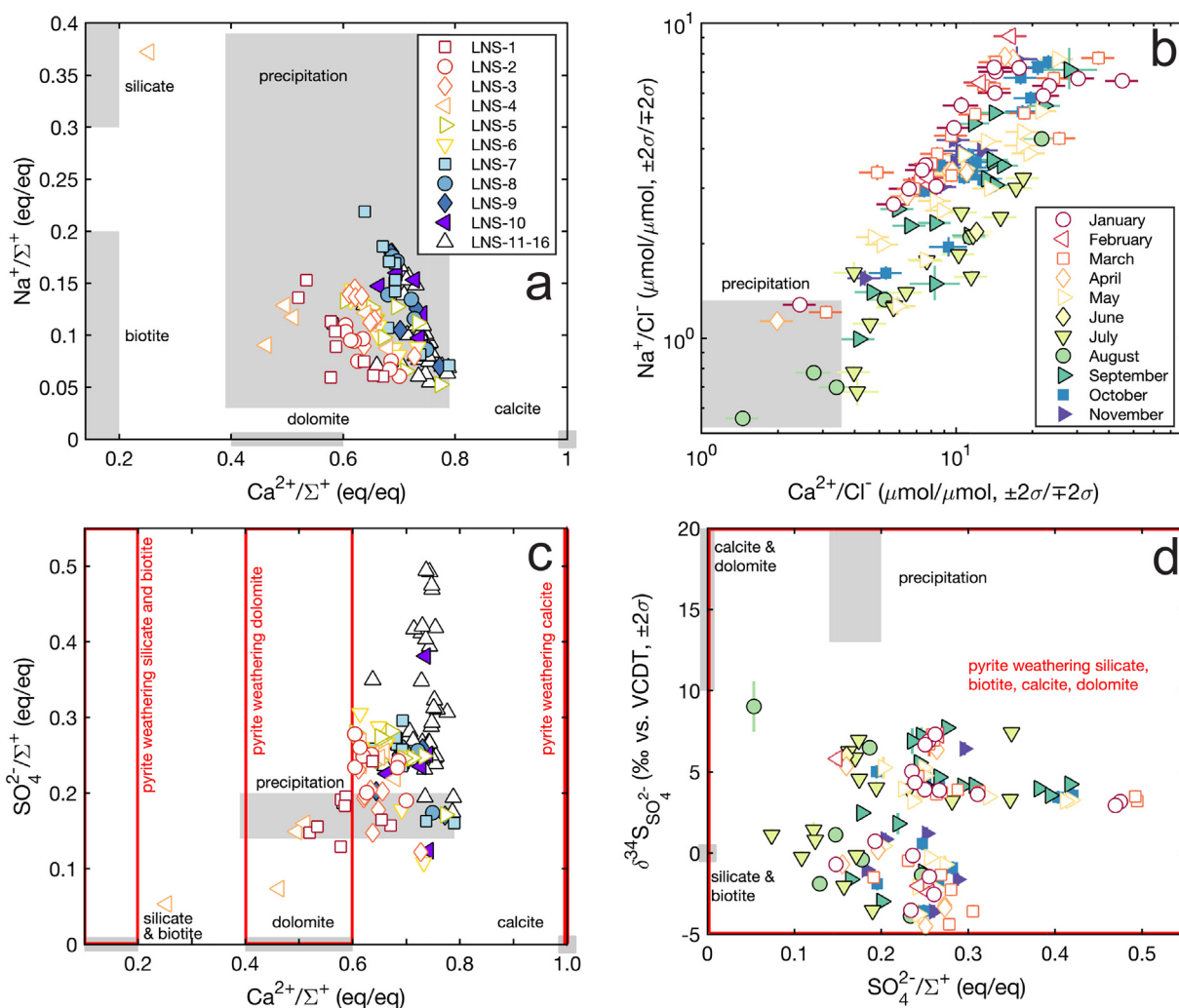

Fig. 6. Mixing diagrams color coded by (a, c) site location, or (b, d) month of collection. (a) The cross plot of Na^+/Σ^+ against Ca^{2+}/Σ^+ indicates that most cation charge is derived from either the carbonate mineral end-members or the precipitation end-member, with a relatively small fraction derived from silicate weathering. (b) The cross plot of Na^+/Cl^- against Ca^{2+}/Cl^- indicates mixing between a high-Cl$^-$ end-member such as precipitation with the low-Cl$^-$ of silicate and carbonate end-members. The two samples not successfully inverted have low Na^+/Cl^- or Ca^{2+}/Cl^- and are out of plotting range. (c) River water samples show SO_4^{2-}/Σ^+ in excess of precipitation. The missing SO_4^{2-} can be provided through FeS$_2$ oxidation and subsequent weathering of carbonate and silicate minerals (red boxes), which sources both SO_4^{2-} and cations to solution. (d) Values of $\delta^{34}S_{SO4}$ are lower than the precipitation or the carbonate end-members. The low $\delta^{34}S_{SO4}$ values could be attained through FeS$_2$ oxidation (red box). For (a)-(d) grey boxes are centered around the mean of end-members distributions and extend 1σ. The red boxes define the mean and 1σ of end-members subject to H$_2$SO$_4$ weathering, although the $\delta^{34}S$ of those end-members is not prescribed during inversion. Although not used in the inversion, for illustrative purposes the $\delta^{34}S$ of the calcite and dolomite end-members are plotted as the range of Phanerozoic evaporites and the $\delta^{34}S$ of the silicate and biotite end-members are plotted as the value of terrestrial sulfur.

and dolomite, river water samples have higher SO_4^{2-}/Σ^+ than can be explained without an additional source of SO_4^{2-} (Fig. 6c). Furthermore, the $\delta^{34}S_{SO4}$ of the samples is lower than the $\delta^{34}S$ values of calcite, dolomite, or precipitation (Fig. 6d). The elevated SO_4^{2-}/Σ^+ and low $\delta^{34}S_{SO4}$ of samples thus require an additional source of ^{34}S-depleted SO_4^{2-}. As previously suggested for the Langtang River (Bhatt et al., 2000, 2018) and shown in the Marsyandi catchment (Turchyn et al., 2013; Hemingway et al., 2020), a likely source of this sulfur is the oxidation of FeS_2. The oxidation of FeS_2 to H_2SO_4 and subsequent weathering of minerals could increase river SO_4^{2-}/Σ^+ and, depending on the value of $\delta^{34}S_{FeS2}$, decrease $\delta^{34}S_{SO4}$ to observed values (Fig. 6c, d, red boxes).

4.2. Sources of dissolved ions

Our inversion model finds that the contribution of each end-member to river chemistry varies by element, site, and season (Figs. 7 and S10). Calcite sources the majority of Ca^{2+} in solution, while Mg^{2+} is sourced from both dolomite and the two silicate end-members. The importance of dolomite weathering increases at the expense of calcite moving downstream (Fig. 7c, d). This shift reflects an increasing influence of LH lithologies, which include massive dolomites, as the river leaves the predominantly silicate mineralogy of the HHC formation (Fig. 1). This observation again demonstrates the first-order control of site location on dissolved chemistry (Bluth and Kump, 1994), consistent with the results of the principal component analysis (Fig. 5).

The silicate end-member and biotite end-member dominate contributions to the budgets of Na^+ and K^+ (Figs. 7a, b and S10). Seasonally, results indicate a strong monsoon increase in weathering of the biotite end-member relative to weathering of the silicate end-member. One explanation for seasonal changes in biotite contribution is changing glacial weathering. Researchers have previously demonstrated that glacial weathering is typically enriched in K^+ and Ca^{2+} (Anderson et al., 1997, 2000). Following mechanical abrasion and the build-up of strain in biotite, K^+ release can occur through leaching or vermiculitization of the damaged mineral lattice. These processes may be exacerbated through either seasonal melting or higher subglacial discharge, explaining the higher biotite contribution during the monsoon. Because the monsoon increase in biotite weathering is reflected across all sample locations, an explanation from glacial weathering would require a meaningful contribution of meltwater to the lower Trisuli River. The monsoon increase in K^+/Σ^+ might alternatively reflect seasonal landslides and the exposure of freshly abraded surfaces (Emberson et al., 2017). Another explanation for the increase in K^+/Na^+ (Fig. 2b) could be a change in clay formation; a simultaneous release from clays of K^+ and Cl^- would explain both the shift towards biotite weathering and the strong covariation of K^+ with Cl^- (Fig. 3). Finally, leucogranites in the Langtang valley have variable K^+/Na^+ ratios, and leucogranites generally show inverse abundances of K^+ and Na^+ (Inger and Harris, 1993). The seasonal shift from the silicate end-member to the biotite end-member in our model results may thus represent a sea-

sonal transition from weathering of HHC gneiss to a high-K^+/Na^+ leucogranite.

4.3. Inversion-constrained fraction of FeS_2-derived SO_4^{2-} and $\delta^{34}S_{FeS2}$

The median fraction of FeS_2-derived SO_4^{2-} ranges from 62% to 101% (Fig. 8a). These findings are consistent with the prior estimate that 70% of $[SO_4^{2-}]$ in this river system derives from FeS_2 oxidation (Galy and France-Lanord, 1999). If this FeS_2-derived SO_4^{2-} had a single characteristic $\delta^{34}S$ across all of our samples, mass balance would result in a clear relationship between the measured $\delta^{34}S_{SO4}$ and the fraction of total SO_4^{2-} attributed to FeS_2 oxidation (Fig. 8b). That is, an increase in the fraction of SO_4^{2-} attributed to FeS_2 oxidation should pull measured $\delta^{34}S_{SO4}$ values towards the $\delta^{34}S$ of the FeS_2 end-member. In contrast, our inversion results do not recover a clear relationship between $\delta^{34}S_{SO4}$ and the fraction of FeS_2-derived SO_4^{2-} at the scale of either individual sampling sites or the entire sample set (Fig. 8b). For example, while station LNS-1 exhibits a range of chemical compositions indicating that 64–93% of SO_4^{2-} is derived from FeS_2 oxidation, varying throughout the year, measured $\delta^{34}S_{SO4}$ remains nearly constant throughout the year at $-1.5 \pm 1.1‰$ (2σ). This result emerges directly from our raw observations of only a weak relationship between $\delta^{34}S_{SO4}$ and Cl^-/SO_4^{2-} (Fig. 4b).

We conclude that our results must be explained by variable $\delta^{34}S$ of FeS_2-derived SO_4^{2-}. Using the model-constrained fraction of FeS_2-derived SO_4^{2-}, measured $\delta^{34}S_{SO4}$, and a range of values of the $\delta^{34}S_{SO4}$ of precipitation (Table 1), we use mass balance to calculate the $\delta^{34}S$ of FeS_2 required by each sample. The uncertainty associated with each determination of $\delta^{34}S_{FeS2}$ reflects the possible range in the fraction of SO_4^{2-} derived from FeS_2 oxidation and uncertainty in the $^{34}S/^{32}S$ ratio of the precipitation end-member. Calculated $\delta^{34}S_{FeS2}$ values fall broadly into two groups (Fig. 8c, d). At station LNS-7 through LNS-16, 80% of the data are explained with median $\delta^{34}S_{FeS2}$ values of 1.7–6.2‰. In contrast, 80% of the data from LNS-1 through LNS-6 are explained with median $\delta^{34}S_{FeS2}$ values of -7.0–0.0‰.

The two groups of samples with distinct $\delta^{34}S_{FeS2}$ values reflect the larger lithological context of the Nepal Himalaya. The catchments of stations LNS-7 through LNS-16 (with 80% of median calculated $\delta^{34}S_{FeS2}$ values between 1.7‰ and 6.2‰) are entirely underlain by HHC, with no exposure of LH or TSS lithologies (Fig. 8d). The FeS_2-derived SO_4^{2-} in the Langtang River is thus likely sourced principally from igneous or metamorphic sulfides in the metapelites and leucogranites of the HHC formation. FeS_2 has been observed as an accessory phase in Langtang rocks (Inger and Harris, 1992; 1993). The isotope composition of igneous sulfide minerals has previously been estimated to range from -10 to $+10‰$ (Thode, 1991; Karim and Veizer, 2000). Overall, the median $\delta^{34}S_{FeS2}$ values of these HHC sites are ^{34}S-enriched relative to bulk Earth and are similar to the average global river $\delta^{34}S_{SO4}$ of approximately 4.5‰ (Macnamara and Thode, 1950; Burke et al., 2018).

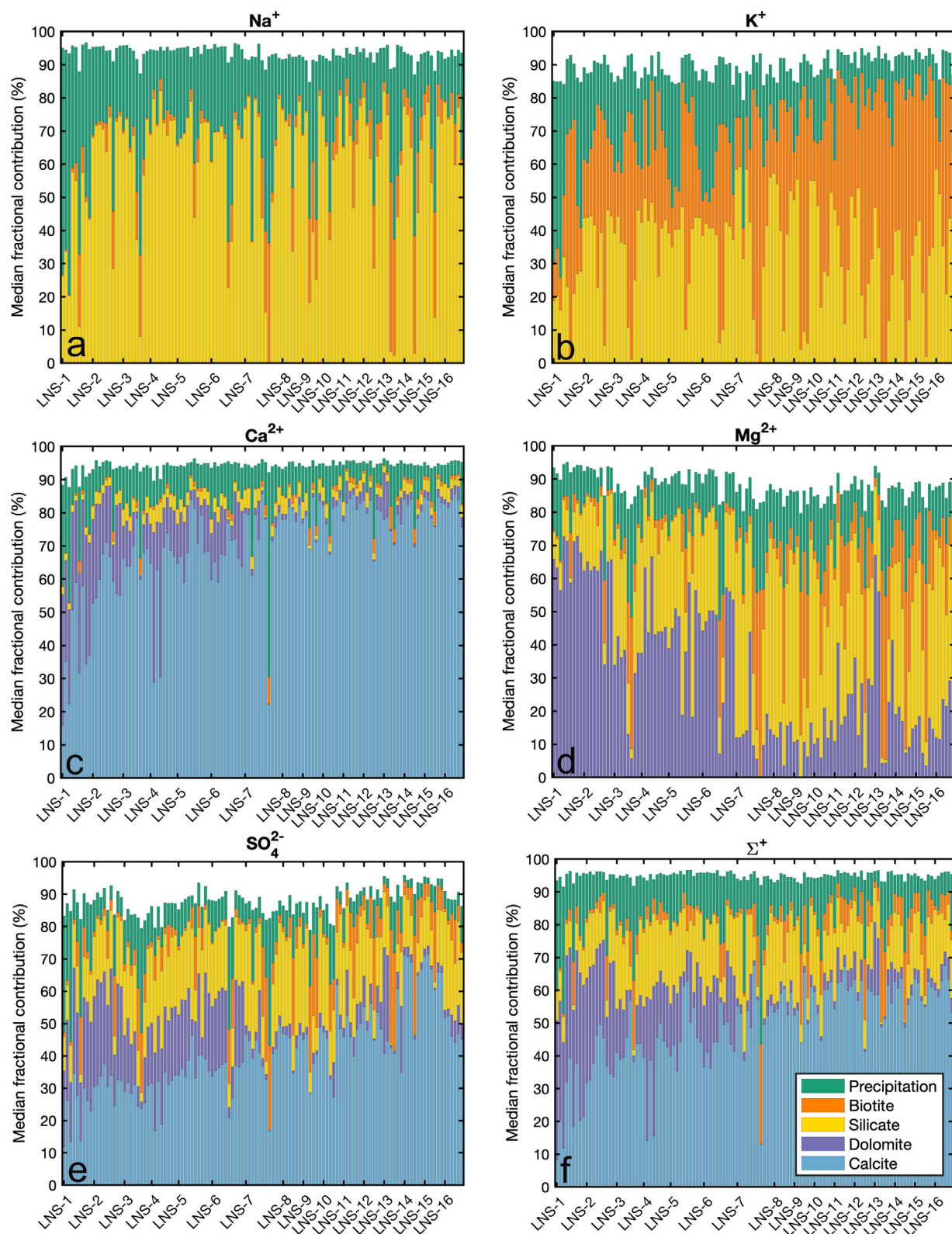Fig. 7. Median fractional contributions of end-members to (a) $[Na^+]$, (b) $[K^+]$, (c), $[Ca^{2+}]$, (d) $[Mg^{2+}]$, (e) $[SO_4^{2-}]$, and (f) $[\Sigma^+]$. Each bar represents a single water sample, organized by collection site, and multiple bars at the same site reflect samples collected in different months. Major trends include a downstream increase in the fraction of Mg^{2+} and SO_4^{2-} sourced from dolomite, as well as seasonal changes in the relative contribution of the silicate and biotite end-members to the budgets of Na^+ and K^+. Although the sum of median contributions is not constrained to equal 100%, in any individual simulation the sum of fractional contributions to each budget must fall between 85% and 115% of observations. Cumulative distribution curves of model results are presented in Appendix 3 (Fig. S10).

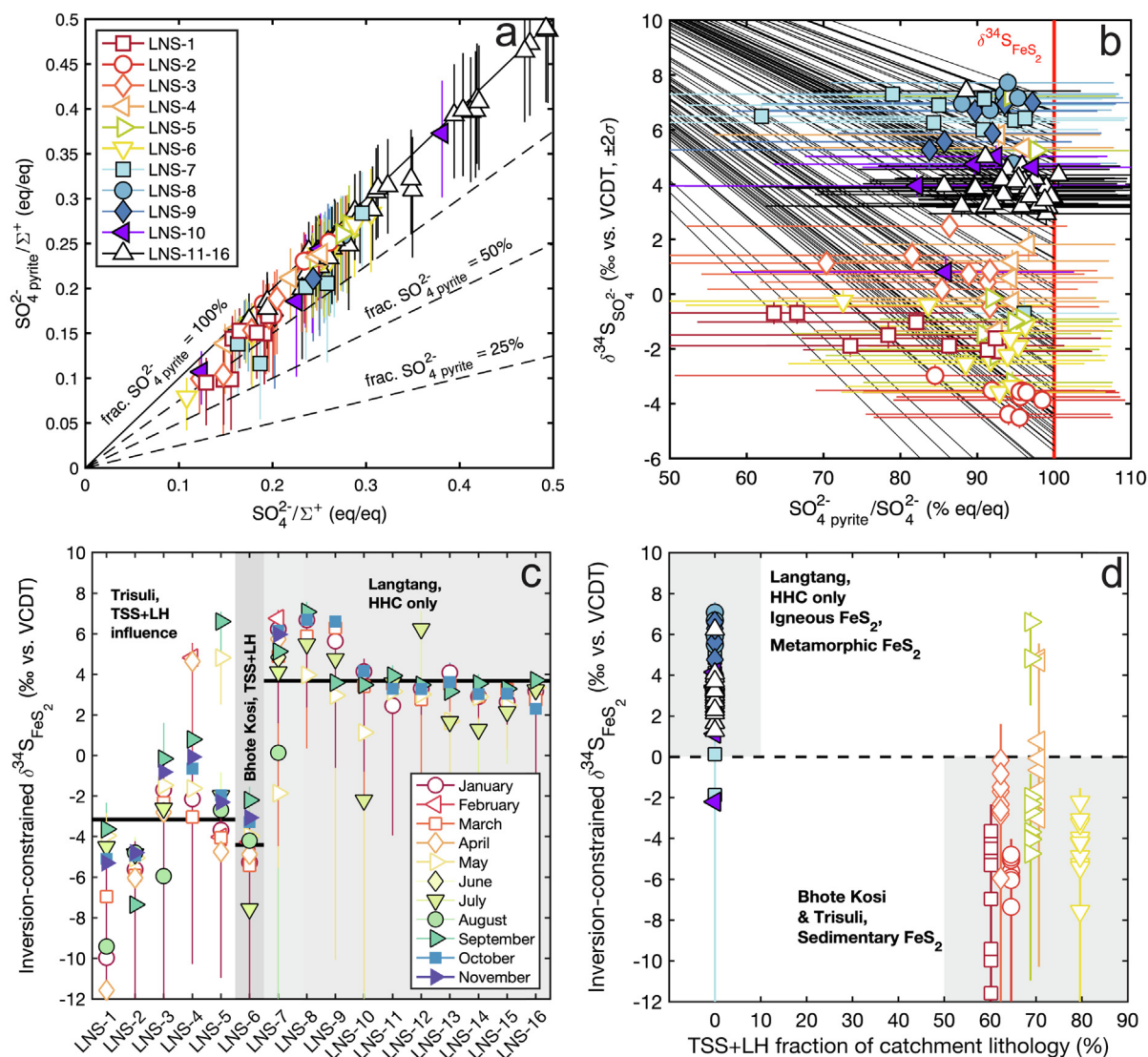Fig. 8. (a) FeS$_2$-derived SO$_4^{2-}$/Σ^+ against observed SO$_4^{2-}$/Σ^+. The Monte Carlo inversion finds that, except for two samples, a median value of 62%-101% of dissolved SO$_4^{2-}$ is derived from the oxidation of FeS$_2$. (b) Measured δ^{34}S$_{SO4}$ and the fraction of FeS$_2$-derived SO$_4^{2-}$. Any relationship between δ^{34}S$_{SO4}$ and the fraction of FeS$_2$-derived SO$_4^{2-}$ is weak. The inversion-constrained δ^{34}S$_{FeS2}$ value is calculated through mass balance and is conceptually similar to the δ^{34}S value at 100% FeS$_2$-derived SO$_4^{2-}$ on a mixing line passing through both the sample and the precipitation end-member (black lines). (c) Inversion-constrained δ^{34}S$_{FeS2}$ against site location shows two distributions. The inversion model recovers a ^{34}S-enriched population in samples draining the HHC formation and an ^{34}S-depleted population for samples with influence from the TSS and LH formations. (d) Inversion-constrained δ^{34}S$_{FeS2}$ against the catchment fraction of TSS and LH. A δ^{34}S$_{FeS2}$ of 0‰ largely separates the two sets of samples. Error bars for model output range from the 5th to 95th percentile of accepted simulation results.

Conversely, the catchments of stations LNS-1 through LNS-6 (with 80% of median calculated δ^{34}S$_{FeS2}$ values between −7.0‰ and 0.0‰) contain substantial outcroppings of the TSS and LH formations (Fig. 8d). As described above, the inversion-constrained values of δ^{34}S$_{FeS2}$ reflect the net δ^{34}S of SO$_4^{2-}$ sourced from both sulfide mineral oxidation and S$_{org}$ oxidation. Because organic matter in the TSS can influence δ^{34}S$_{FeS2}$, the shift in δ^{34}S$_{FeS2}$ relative to LNS-7 through LNS-16 may reflect either a change in the δ^{34}S of weathering sulfide minerals or possibly the oxidation of ^{34}S-depleted S$_{org}$ that was not present in HHC bedrock. Given that organic matter tends to have a

molar C$_{org}$: S$_{org}$ ratio of approximately 100:1, sourcing any consequential fraction of dissolved [SO$_4^{2-}$] from oxidation of organic matter entails a large flux of carbon. Attributing 100% of [HCO$_3^-$] to organic matter oxidation at stations LNS-1 through LNS-6 would explain only 4–25% of [SO$_4^{2-}$], strongly suggesting that most river SO$_4^{2-}$ is not derived from S$_{org}$ oxidation. Furthermore, major ion concentrations and prior measurements of DIC δ^{13}C (Galy and France-Lanord, 1999) both indicate that carbonate weathering is a significant source of HCO$_3^-$. However, because CO$_2$ can be lost from river systems through degassing (Raymond et al., 2013), the relative abundance of DIC

and SO_4^{2-} would not be expected to strictly match the C_{org}:S_{org} ratio of organic matter. Moreover, gas exchange can offset DIC $^{13}C/^{12}C$ from the primary carbon isotope ratio in organic matter. While a contribution from S_{org} oxidation to river SO_4^{2-} in the Langtang-Trisuli-Narayani River system is thus still possible, it is more parsimonious to attribute the downstream shift in $\delta^{34}S_{FeS2}$ to a change in the $\delta^{34}S$ of weathering sulfide minerals. Sedimentary pyrites tend to have low $\delta^{34}S$ values due to their formation by the fractionating process of microbial sulfate reduction (Thode et al., 1951; Sim et al., 2011), and could feasibly be ^{34}S-depleted relative to the sulfide minerals of the HHC formation. Previous work in the Marsyandi river has shown that SO_4^{2-} derived from FeS_2 oxidation in the TSS reaches $\delta^{34}S$ values as low as approximately −25‰, consistent with but lower than our minimum estimates of $\delta^{34}S_{FeS2}$ in downstream stations (Turchyn et al., 2013; Hemingway et al., 2020).

Our findings are similar to prior observations from the Indus River Basin where a decline in $\delta^{34}S_{SO4}$ from headwater to lowland samples was likewise attributed to a transition from weathering igneous and metamorphic sulfide minerals to the weathering of sedimentary sulfide (Karim and Veizer, 2000). Similarly, our results are in agreement with the finding that weathering of magmatic sulfides may impact dissolved chemistry in the Marsyandi River downstream of the TSS (Turchyn et al., 2013). However, our measurements emphasize the possibility that, as previously considered and rejected in Turchyn et al. (2013), a second FeS_2 end-member with relatively high $^{34}S/^{32}S$ ratio, or alternatively a range of end-members with variable $^{34}S/^{32}S$ ratios, may contribute to the observed rise in $\delta^{34}S_{SO4}$ within the TSS section of the Marsyandi River.
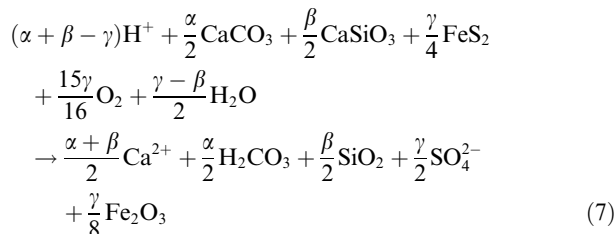
4.4. Carbon cycle implications of weathering in the Langtang-Trisuli-Narayani River system

Weathering of carbonate and silicate minerals by H_2CO_3 or H_2SO_4 has distinct impacts on the fluxes of ALK and DIC. After formalizing a framework introduced in Torres et al. (2016) we apply this methodology to show that weathering in the Langtang-Trisuli-Narayani River system is not a source or sink of CO_2 over timescales greater than marine carbonate compensation (5–10 kyr) (Archer et al., 1997, 2000) and shorter than the marine SO_4^{2-} residence time (approximately 10 Myr).

4.4.1. Impacts of sulfuric acid weathering on ΔALK and ΔDIC

The chemical weathering of carbonate and silicate minerals can be described as titration reactions (Eqs. (1) and (4)) where the source of H^+ can be either H_2CO_3 or H_2SO_4 (Eq. (5)). Because the chemical reactions are written with each chemical species in the dominant form it would take at the CO_2 equivalence point, the ΔALK and ΔDIC of each equation are the stoichiometric factors on H^+ and H_2CO_3, respectively (Zeebe and Wolf-Gladrow, 2001). Taking β and α to represent the production of ALK through silicate (Eq. (1)) and carbonate weathering (Eq. (4)), respectively, and γ the consumption of ALK through

FeS_2 oxidation by reduction of O_2 (Eq. (5)), a generic weathering reaction is constructed from their weighted sum (Eq. (7)). This net reaction shows that $\Delta ALK = \alpha + \beta - \gamma$ and $\Delta DIC = \alpha/2$. Note that, unlike Torres et al. (2016), here we do not require the explicit coupling of H^+ production and H^+ consumption. Because α and β reflect the flux of ALK and not Ca^{2+} specifically, these formulations of ΔALK and ΔDIC are general across mineral stoichiometries.

$$(\alpha + \beta - \gamma)H^+ + \frac{\alpha}{2}CaCO_3 + \frac{\beta}{2}CaSiO_3 + \frac{\gamma}{4}FeS_2$$
$$+ \frac{15\gamma}{16}O_2 + \frac{\gamma - \beta}{2}H_2O$$
$$\rightarrow \frac{\alpha + \beta}{2}Ca^{2+} + \frac{\alpha}{2}H_2CO_3 + \frac{\beta}{2}SiO_2 + \frac{\gamma}{2}SO_4^{2-}$$
$$+ \frac{\gamma}{8}Fe_2O_3 \tag{7}$$

The parameter R is defined as the ratio of carbonate weathering to total weathering (Eq. (8)) and is equal to $\frac{\alpha}{\alpha+\beta}$. The parameter Z is defined as the fraction of weathering done with H_2SO_4 (Eq. (9)) and is equal to $\frac{\gamma}{\alpha+\beta}$. The fraction of silicate weathering to total weathering is 1-R, and the fraction of CO_2-driven weathering is 1-Z. Following inversion, R and Z can be defined explicitly as the sum of ionic contributions from each of the four lithologic end-members in our inversion (Eqs. (8) and (9)). Brackets in Eqs. (8) and (9) indicate the concentration of the indicated element that can be attributed to the subscripted end-member, and factors convert concentrations to units of charge equivalents. The numerator of R is thus the sum of Ca^{2+} and Mg^{2+} contributions from calcite and from dolomite, and the numerator of Z is the sum of SO_4^{2-} contributions from each of the four non-precipitation end-members, shown as the sum over the ith end-member. Lastly, the denominator of both R and Z is the sum of Ca^{2+}, Mg^{2+}, Na^+, and K^+ contributions from each of the 4 weathering end-members, also shown as a sum over the ith end-member. The net ΔALK/ΔDIC due to a weathering system can then be calculated as a simple function of R and Z.

$$R = \frac{\alpha}{\alpha + \beta}$$
$$= \frac{\left(2 * [Ca^{2+}]_{calcite} + 2 * [Ca^{2+}]_{dolomite} + 2 * [Mg^{2+}]_{dolomite}\right)}{\Sigma_{i=1}^{4}(2 * [Ca^{2+}]_i + 2 * [Mg^{2+}]_i + [Na^+]_i + [K^+]_i)} \tag{8}$$

$$Z = \frac{\gamma}{\alpha + \beta}$$
$$= \frac{\Sigma_{i=1}^{4}(2 * [SO_4^{2-}]_i)}{\Sigma_{i=1}^{4}(2 * [Ca^{2+}]_i + 2 * [Mg^{2+}]_i + [Na^+]_i + [K^+]_i)} \tag{9}$$

When viewed instantaneously, any flux with ΔALK/ΔDIC > 1 will sequester CO_2 into the ocean while fluxes with ΔALK/ΔDIC < 1 will source CO_2 to the atmosphere. The boundary for this instantaneous CO_2 flux is Z = 1 − R/2 (Eq. (10)). The influence of chemical fluxes on pCO$_2$ over longer timescales depends on the removal rate of individual ions from the global ocean–atmosphere system. Because the reduction of SO_4^{2-} in marine sediments

consumes H^+ and counteracts the ALK flux of terrestrial FeS_2 oxidation, FeS_2 oxidation during weathering influences climate on timescales shorter than the ~10 Myr marine residence time of SO_4^{2-}. During a transient period of time in which sulfide oxidation increases pCO_2, marine SO_4^{2-} concentrations increase in tandem (Torres et al., 2014; Rennie et al., 2018). Carbonate mineral burial ultimately removes most of the alkalinity supplied to the global ocean from rivers, so a second relevant timescale is that of carbonate compensation. Because carbonate mineral burial removes ALK and DIC in a 2:1 ratio, fluxes with ΔALK/ΔDIC < 2 represent sources of CO_2 to the atmosphere on timescales longer than carbonate compensation but shorter than the marine SO_4^{2-} residence time. The boundary for this long time-scale CO_2 flux is Z = 1-R, which implies that fluxes with $1 < \Delta$ALK/ΔDIC < 2 are short-term sinks of atmospheric CO_2 but long-term sources (Torres et al., 2016) (Eq. (10)).

$$\frac{\Delta ALK}{\Delta DIC} = \frac{(\alpha + \beta - \gamma)}{\alpha/2} = 2\left(\frac{\frac{\alpha+\beta-\gamma}{\alpha+\beta}}{\frac{\alpha}{\alpha+\beta}}\right) = 2\left(\frac{1-\frac{\gamma}{\alpha+\beta}}{\frac{\alpha}{\alpha+\beta}}\right)$$
$$= 2\frac{(1-Z)}{R} \qquad (10)$$

4.4.2. R and Z in the Langtang-Trisuli-Narayani River system

Except for one low value of R and two samples without successful inversion results, the median fraction of cations sourced from carbonate end-members in our samples ranges between 60% and 86% (Fig. 9). These values are consistent with previous studies of the Langtang-Trisuli-Narayani River system (West et al., 2002; Tipper et al., 2006; Galy and France-Lanord, 1999). The median fraction of weathering acid sourced from FeS_2 oxidation ranges from 10% to 55%, similar to values calculated for the Andean middle mountains and floodplain of southern Peru (Torres et al., 2016). Values of R and Z in the Langtang-Trisuli-Narayani River system exhibit both seasonal and spatial trends, but overall the data scatter around the line Z = 1 − R (Figs. 9a, b, S11, and S12). As discussed above, the line Z = 1 − R corresponds to ΔALK/ΔDIC = 2 (Eq. (10)) and defines the line across which chemical weathering has no implications for the carbon cycle on timescales greater than 5–10 kyr and less than approximately 10 Myr. Our data thus straddle the line between long-term sources and sinks of pCO_2; we conclude that, within uncertainty, FeS_2 oxidation in the Narayani River catchment may completely compensate for the canonical pCO_2 drawdown of silicate weathering. However, the spatial and seasonal changes in R and Z do shift whether the instantaneous flux is a source or sink of CO_2. Understanding the origin of this chemical variability is critical for characterizing how the global carbon cycle has responded to Himalayan weathering throughout the Cenozoic.

4.4.2.1. Spatial changes in R and Z.
The inversion results indicate minimal spatial variation in the fraction of carbonate weathering (R) (Fig. 9c). This lack of downstream variation is unexpected given the change in lithology from the silicate-dominated HHC to the dolomite-rich LH (Figs. 1 and S13). The lack of clear trend may reflect the supersaturation of Himalayan waters with respect to calcite, such that any downstream change in the magnitude of carbonate weathering is obscured by secondary carbonate precipitation (Bickle et al., 2015). An alternative explanation is that enhanced carbonate weathering associated with the transition to a dolomite-rich lithology is compensated by enhanced weathering of silicates as the river moves into a warmer and wetter environment (West et al., 2002).

In contrast, the fraction of acid sourced through FeS_2 oxidation (Z) decreases downstream (Fig. 9d). The mean Z value of the Lirung Glacier sites is 35%, decreasing to a mean value of 28% at LNS-7 and LNS-8 in the downstream Langtang, and reaching a mean value of 23% in the lowermost 4 sampling sites. The downstream decrease in the fraction of sulfuric acid weathering reflects the transition from a mountainous, highly erosive regime to a flatter environment with limited access to primary FeS_2 from bedrock erosion. The highest values of Z are found in glacial catchments, consistent with prior observations from glacial rivers (Anderson et al., 2000; Emberson et al., 2017) and inversion of global data (Torres et al., 2017). This effect can be explained because glaciers generate enhanced mineral surface area and disproportionately express weathering reactions with rapid kinetics, such as sulfide oxidation and carbonate dissolution (Gabet et al., 2008; Tranter and Wadham, 2014; Torres et al., 2017). The net effect of the consistently elevated Z values for some of our sampling sites in the headwaters, e.g., in the upper Langtang valley, together with little difference in R, is that these locations lie within the R-Z space characterized by long-term CO_2 release, even though the Narayani system as a whole falls in the region where sources and sinks are approximately balanced.

4.4.2.2. Seasonal changes in R.
Prior studies have identified an increase in the fraction of carbonate weathering during the monsoon season in several sites throughout the Narayani River system, including the Lirung Glacier outlet within the upper Langtang Valley (Bhatt et al., 2000; Tipper et al., 2006), four sites in the Marsyandi basin with detailed time series data (Tipper et al., 2006), a series of small TSS-draining tributaries in the Marsyandi catchment with paired April/May and September samplings (Bickle et al., 2005; Tipper et al., 2006), the Trisuli River sampled at Betrawati (equivalent to our site LNS-4; Galy and France-Lanord, 1999), and the greater Ganges rivers (Sarin et al., 1989). One explanation for the observed seasonal increase in the fraction of carbonate weathering is a hydrological transition in which, during the monsoon season, flow paths with shorter residence times become relatively more important than during the non-monsoon season (Tipper et al., 2006).

Due to the rapid dissolution kinetics of carbonate mineral relative to the slow dissolution kinetics of silicate minerals, a parcel of water given longer time for water–rock interaction may accumulate a larger fraction of silicate-derived cations (Tipper et al., 2006). As a result, water sourced from deeper flow paths with a longer residence time
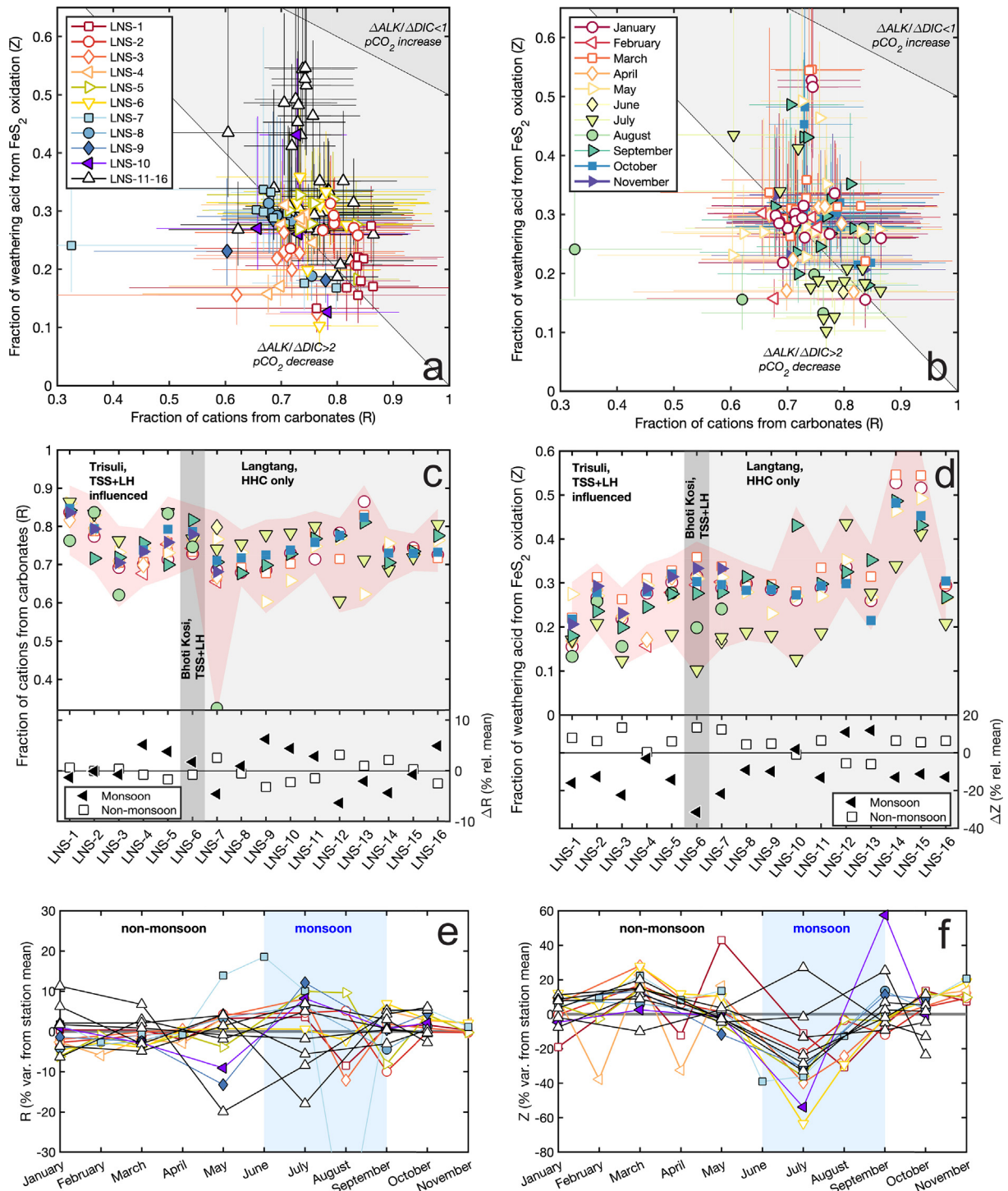
Fig. 9. (a, b) Fraction of weathering acid sourced from FeS_2 oxidation (Z) against the fraction of carbonate weathering (R), coded by (a) sample site or (b) month of collection. Most data cluster around $Z = 1 - R$, the boundary between short-term and long-term CO_2 release. (c) R arranged by site location and coded by season. Inversion results do not show clear spatial or seasonal changes. (d) Z arranged by site location and coded by season. Inversion results show a downstream decline in sulfuric acid weathering, and samples from the monsoon season generally have lower Z values than those from the non-monsoon season. In (c) and (d) samples are also aggregated as belonging to either the monsoon season (June through September, black triangles) or non-monsoon season (other months, white squares) and are plotted relative to the mean of the median R or Z values at each location. (e) Timeseries of variations in R relative to the annual station mean. R does not strongly covary with season. (f) Timeseries of variations in Z relative to the annual station mean. The value of Z is reduced during the monsoon at most sampling sites. In (e) and (f), blue shading indicates the monsoon season. Error bars for model output range from the 5th to 95th percentile of accepted simulation results. (For interpretation of the references to color in this figure legend, the reader is referred to the web version of this article).

can be expected to have a larger fraction of silicate-derived cations. As the monsoon seasons begins and the water table rises, the source of water in the river channel may become dominated by flow paths with shorter residence times, potentially at shallower depths, and may thus express a higher fraction of carbonate-derived cations. In turn, the fraction of carbonate weathering may decline as the monsoon season wanes and deeper flow-paths with longer residences times increase their fractional contribution to water in the river channel (Tipper et al., 2006). This hydrological explanation for seasonal changes in the carbonate weathering ratio relies on changes in the ratio of water sourced from shallow flow paths to total discharge; this ratio may increase or decrease even if the absolute quantity of water sourced from both shallow and deeper flow paths increases due to intense monsoon precipitation, an elevated groundwater table, and an increase in hydraulic head.

Unlike prior work, our analysis does not recover clear seasonal changes in R (Fig. 9c, e); this finding is seen when model results are plotted for individual months against sampling location (Fig. 9c top, colored symbols), clustered into those belonging to either the monsoon season (June–September) or the non-monsoon season (January through May and October through November) (Fig. 9c bottom, black and white symbols), or as a timeseries (Fig. 9e). Although we do not have discharge measurements at all stations, we consider the values of R for different relative discharges using a synthetic hydrograph (Fig. S7). Opposite to expectations from prior findings, regressions of R against the synthetic discharge curve do not show consistently positive relationships (Fig. 10). Thus, when considering all of the major ion concentration measurements (Fig. 9c, e), we do not recover the monsoon increase in R reported in previous work (Sarin et al., 1989; Tipper et al., 2006) (Fig. S14).

Application of our inversion calculation to previously published datasets shows that the lack of seasonality in R

is not simply a result of the modeling approach we use (Fig. S14): our inversion model recovers monsoon increases in R for samples of the Trisuli River at Betrawati reported in Galy and France-Lanord (1999) (Fig. S14a) and in the Lirung Glacier outflow data of Bhatt et al. (2000) (Fig. S14d). Conversely, we find only minimal seasonal changes in R for the time-series data of Tipper et al. (2006) from tributaries of the Marsyandi River (Fig. S14g). However, the evidence for seasonal changes in carbonate weathering reported in Tipper et al. (2006) is primarily based on observations of $Si(OH)_4/Ca^{2+}$ ratios and $^{87}Sr/^{86}Sr$ ratios, yet neither [Si] nor $^{87}Sr/^{86}Sr$ ratios are included in our inversion model (Fig. S14g, h). A second potential reason for this disagreement is that the Marsyandi catchment contains hot springs that may source Cl^- to the river, which are also not included in our primary inversion (Figs. S4 and S16), and thus the contribution of precipitation to the dissolved load may be overstated in our treatment of the data from Tipper et al. (2006).

If observations of $[K^+]$ and $[Cl^-]$ are removed from the inversion, we do recover a clear seasonal increase in the fraction of carbonate weathering, broadly similar to that seen in prior work (Appendix 4, Fig. S17). The key difference between our results and those reported previously is thus our observation of elevated K^+/Σ^+ during the monsoon season (Fig. 3d), which sustains the silicate weathering contribution to the solute load. This relative invariance of $[K^+]$ during the monsoon season (i.e., lack of dilution as seen for other solutes including $[Ca^{2+}]$) has been not documented in prior studies from the Nepal Himalaya. One explanation for our observation that K^+ behavior differs from that found in previous work could be that the processes responsible for sourcing K^+ have strengthened with time, for example if preferential leaching from glacially-ground minerals has become more efficient as glaciers have retreated. Such a change in weathering dynamics might explain why samples collected in the 1990s and early 2000s did not capture the effect that we see in samples from 2011, with potentially important implications for how changes in glacial dynamics over decadal timescales affect solute chemistry. Alternatively, we recognize that our observations of elevated $[K^+]$ may be an experimental artifact of bottle washing or sample collection. Notably, inclusion of hot springs in the inversion results in a monsoon decrease in carbonate weathering fraction, opposite to prior findings (Fig. S16), while inclusion of an evaporite end-member does not meaningfully change our results (Fig. S15). Likewise, the results of our primary inversion model are similar to those of a simple forward model (Fig. S18). In all cases, further study is warranted on the seasonally changing solute chemistry in rivers fed by Himalayan glaciers.

4.4.2.3. Seasonal changes in Z. Seasonal shifts in Z are more pronounced than those in R in our data, with the Z value of a given location lower during the monsoon season than during the non-monsoon (Fig. 9d, f). This monsoon decline in the proportion of solutes from H_2SO_4-driven weathering is seen in 13 out of 16 stations and has an absolute magnitude of 1–13%, corresponding to a 3–40% relative change in
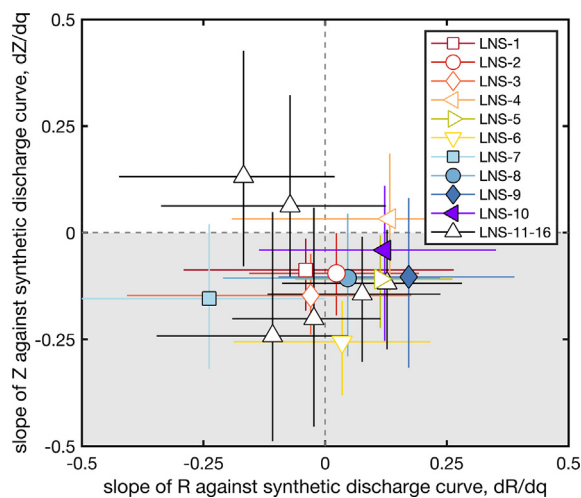

Fig. 10. Regression of R against the monthly fraction of maximum annual discharge shows positive and negative slopes, while regression of Z shows mostly negative slopes. Grey shading indicates the region with dZ/dq < 0. Error bars on dR/dq and dZ/dQ reflect the 5th to 95th percentile of Monte Carlo modeling for the regression slope of R or Z against a synthetic discharge curve (Fig. S7).

the fraction of weathering driven by H_2SO_4 (Fig. 9d). This seasonal change in Z is larger in the TSS-influenced sites than in the HHC-influenced sites. One consequence of the observed seasonality is that the fraction of H_2SO_4-driven weathering declines with higher fractional discharge (Fig. 10).

Our results agree with those reported for the Trisuli River by Galy and France-Lanord (1999), who report a seasonal decline in the ratio of SO_4^{2-} from sulfide oxidation and evaporite dissolution relative to the sum of total SO_4^{2-} and HCO_3^-. Application of our inversion model to their data recovers a monsoon-season decrease in Z (Fig. S14b). A monsoon decrease in Z is also recovered in data from the Lirung Glacier outlet reported by Bhatt et al. (2000) (Fig. S14e) and in the Chame and Nar Khola timeseries data from Tipper et al. (2006) (Fig. S14h).

Explanations for seasonal changes in Z depend on the subsurface structure of chemical weathering fronts, which are themselves determined by the long-term interaction of tectonics and weathering. Without additional observations of the FeS_2 and $CaCO_3$ weathering profiles in our sampling catchments, at this time we can only hypothesize as to the relevant mechanisms driving the observed seasonal solute dynamics. Below, we briefly evaluate the consistency of our observations with different erosional scenarios (Fig. 11).

When the residence time of a mineral in the weathering zone is short relative to the time required for weathering, insufficient time for complete dissolution prevents the development of a complete subsurface dissolution front (i.e., the zone where mineral abundances decline to zero; Brantley and Lebedeva, 2011). This regime, termed "kinetic limitation", contrasts with "supply limitation" wherein sufficient time is available for weathering such that the mineral abundances decline to zero below the weathering zone surface. Holding all other factors equal, minerals will transi-

tion from supply limitation to kinetic limitation as the erosion rate increases owing to a faster transit through the weathering zone (West, 2012). The exact crossover point between kinetic limitation and supply limitation varies among minerals depending upon their reactivity and abundance in the weathering zone; a reasonable expectation is that reactive minerals will remain supply limited over a larger range of erosion rates than will less reactive minerals (Gu et al., 2020). Under supply limitation, the position of a subsurface dissolution front may still shoal with increasing erosion.

When the residence time of FeS_2 in the weathering zone is relatively long, there may be sufficient time for the development of a deep FeS_2 dissolution front (Fig. 11, purple FeS_2 front). In this case, shallow flow paths would have minimal access to FeS_2 while deeper flow paths could accumulate SO_4^{2-} through FeS_2 oxidation. During the higher discharge of the monsoon season, an increase in the fraction of river channel water derived from shallower flow paths above a deep FeS_2 weathering front would lead to a seasonal reduction in the Z value recorded by the river chemistry. That is, enhanced discharge would result in a lower observed fraction of weathering driven by H_2SO_4, consistent with our observations (Fig. 9 and 10). Although a deep FeS_2 weathering front is difficult to reconcile with the high erosion rates of the Himalaya, much of the weathering in rapidly-eroding mountain belts takes place in bedrock, as opposed to soil profiles, and with influences from groundwater (Andermann et al., 2012; West, 2012).

When erosion rates are very high, FeS_2 may remain supply limited while only being depleted in a thin near-surface zone (Fig. 11, blue FeS_2 front). Under this condition, where all flow paths would have access to FeS_2, seasonal transitions in the source of water entering the river channel are unlikely to explain the observed seasonality in Z. In this
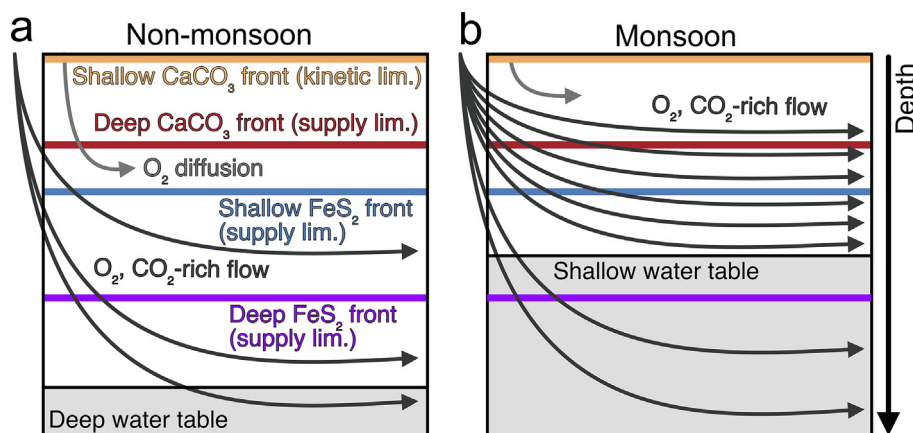

Fig. 11. Schematic of seasonal weathering cycle with two possible positions for the $CaCO_3$ weathering front (orange, red) and FeS_2 weathering front (blue, purple). During all seasons O_2 and CO_2 reach the subsurface from both diffusive exchange with the atmosphere and advection of waters (Brantley et al., 2013). (a) Deep flow paths with long residence times accumulate SO_4^{2-} from FeS_2 oxidation and source water to the river channel during the non-monsoon. (b) During the monsoon, the ratio of water in the river channel sourced from shallow flow paths with shorter residence times may increase even as the absolute discharge through both shallow and deep flow paths increases. If the FeS_2 weathering front is deep (purple, lower erosion rates), a seasonal change in the contributions of flow paths with distinct residence times could cause lower Z values in river samples. If the FeS_2 weathering front is shallower (blue, higher erosion rates), a transition in the hydrology of the system may not explain the observed seasonality of Z, which could instead reflect seasonal changes in the chemistry of water in flow paths with short residence times. (For interpretation of the references to color in this figure legend, the reader is referred to the web version of this article.)
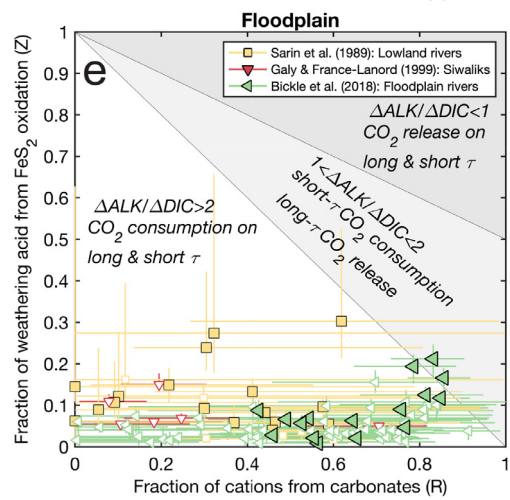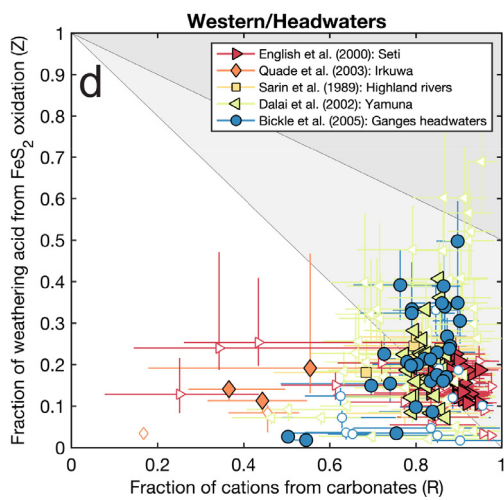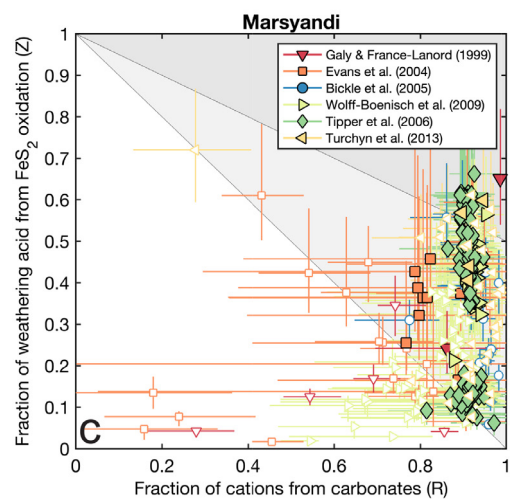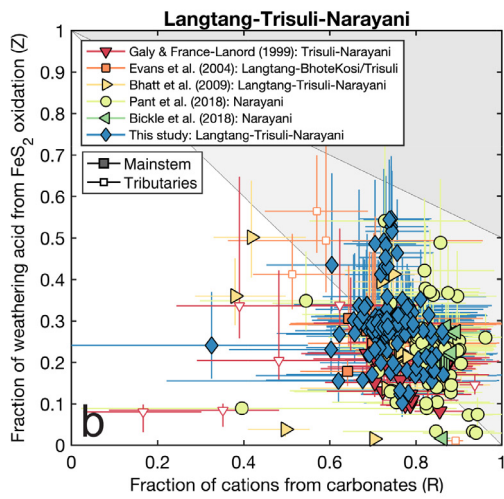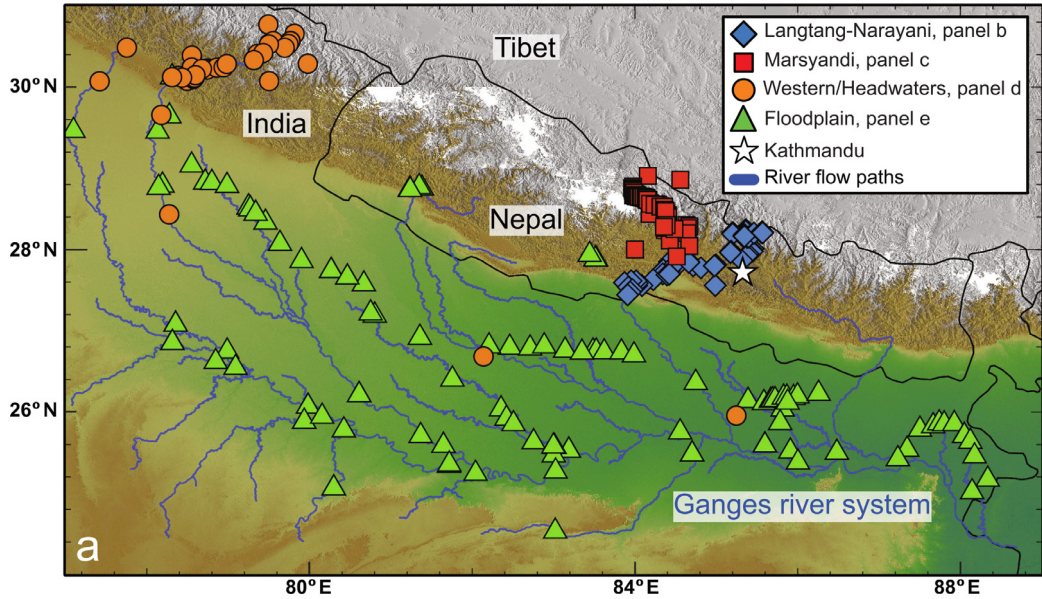
Fig. 12. (a) Sample locations from prior publications reporting the dissolved chemistry of Himalayan rivers. Water chemistry is inverted and presented in subsequent panels even if detailed location data are unavailable. Latitude and longitude for samples from Sarin et al. (1989) and Galy and France-Lanord (1999) were estimated using Google Earth. The two Western/Headwater samples that appear in the floodplain are Highland Rivers from Sarin et al. (1989). Elevation data are from the Shuttle Radar Topography Mission. (b)–(e) Fraction of weathering acid sourced from FeS_2 oxidation (Z) against the fraction of carbonate weathering (R) grouped by location and coded by publication. Data are shown for both mainstem (closed symbols) and tributary samples (open symbols), as identified in original publications. Shading indicates regions of $\Delta ALK/\Delta DIC < 1$, $1 < \Delta ALK/\Delta DIC < 2$, and $\Delta ALK/\Delta DIC > 2$, with different implications for pCO_2 drawdown over short and long timescales (τ). (b) Langtang-Trisuli-Narayani River system samples tend to cluster around the line $Z = 1 - R$, indicating that sulfide oxidation offsets much of the CO_2 drawdown associated with silicate weathering. (b) Marsyandi samples have high Z and high R values consistent with long-term CO_2 supply to the atmosphere. Samples draining the TSS are particularly high in Z. (c) Samples from the western headwaters of the Ganges and the Seti River are chemically similar to those from the Trisuli-Narayani catchment. (d) Samples from the floodplain have low Z and low R values, indicative of silicate weathering driven predominantly with H_2CO_3 (Lupker et al., 2012; Bickle et al., 2018). Error bars for model output range from the 5th to 95th percentile of accepted simulation results.

case, an alternative explanation for observed seasonality comes from considering the changing supply of CO_2 and O_2 to the weathering system. During periods of high precipitation, an enhanced flux of CO_2 and O_2 are supplied to the subsurface for potential consumption in weathering reactions. If the waters hosting such weathering reactions are rapidly exported into the channel, this seasonal supply of acids and oxidants could influence the observed values of R and Z. When a seasonal flux of oxidant does not reach the FeS_2 weathering front, the seasonal reduction in Z could be caused by an increase in H_2CO_3-driven weathering (Winnick et al., 2017). Alternatively, if the FeS_2 front is shallow, seasonal increases in the supply ratio of CO_2/O_2 could induce depletions in Z; such an increase could be due to the oxidation of organic carbon formed during the non-monsoon season. In these cases, the observed changes in Z would result from altering the chemistry of water in shallow flow paths rapidly exported to the river channel, as opposed to changing the relative contributions of water from different hydrologic regions.

4.4.3. Extension to geologic timescales

The tectonic and erosional dynamics of the weathering system impact how seasonal changes might be representative of climate changes over longer timescales. When extrapolated beyond seasonal timescales, our observations of seasonal change in Z ostensibly could indicate a negative feedback between discharge and FeS_2 oxidation (Fig. 10). Climate models show that global warming is associated with a strengthened hydrologic cycle and location-specific changes in runoff (Otto-Bliesner, 1995). Thus, if the patterns we observe are representative of responses over long timescales, then higher temperatures forced by higher pCO_2 could result in greater discharge, lower fractions of FeS_2 oxidation, and a more effective silicate weathering cycle. Preliminary evidence for such a feedback can be found in the Cenozoic increase of dissolved marine $[SO_4^{2-}]$ during the corresponding decline in pCO_2 inferred from $CaCO_3$ $\delta^{18}O$ (Zachos et al., 2001; Horita et al., 2002; Torres et al. 2014). However, the feedback between discharge and H_2SO_4-driven weathering relies on the supply of O_2 and CO_2 relative to the position of the water table and relative to the FeS_2 and $CaCO_3$ weathering fronts (Fig. 11). Although presumably stable on the decadal timescales of concentration-discharge observations, this weathering

dynamic is likely to shift due to long-term changes in tectonics and climate (Godsey et al., 2009, 2019; Ibarra et al., 2016). For example, if we assume that erosion rates balance uplift rates over tectonic timescales, the long-term control of Himalayan sulfide oxidation is likely to be tectonic shortening rather than river discharge. Indeed, the interplay between seasonal weathering dynamics and discharge likely changed throughout the uplift of the Himalaya and the initiation and development of the seasonal monsoon.

4.5. Inversion of published river observations from the Nepal Himalaya

Prior datasets of dissolved river chemistry from throughout the Nepal Himalaya were inverted using the same model applied to our samples from the Langtang-Trisuli-Narayani River system (Fig. 12; Table 1). The inverted data come from the Langtang River (Bhatt et al., 2009), the Marsyandi catchment (Bickle et al., 2005; Tipper et al., 2006, Wolff-Boenisch et al., 2009; Turchyn et al., 2013), the Yamuna catchment (Dalai et al., 2002), the greater Narayani basin (Galy and France-Lanord, 1999; Pant et al., 2018), rivers of the western Himalayan (English et al., 2000; Quade et al., 2003), and the Ganges floodplain rivers (Sarin et al., 1989; Bickle et al., 2018) (Fig. 12a). Analogous to our samples from the Langtang-Trisuli-Narayani River system, the larger dataset reveals that carbonate weathering sources the majority of cations to solution, and there is strong evidence of extensive weathering driven by H_2SO_4 (Fig. 12b, c, d, e).

Overall, analysis of R and Z in the previously published data reveals a transition from weathering as CO_2-neutral in the mountainous fronts of the Himalaya (Fig. 12b, c, d) to weathering as a sink of CO_2 in the floodplain (Fig. 12e). Samples from prior study of the Langtang-Trisuli-Narayani River system are similar to those reported here and show that FeS_2 oxidation largely offsets CO_2 drawdown due to silicate weathering throughout the Narayani catchment. In a few cases, similar to the Langtang headwaters in our study, mountainous sites are characterized by long-term CO_2 release. Conversely, samples from the Ganges floodplain (Sarin et al., 1989; Galy and France-Lanord, 1999; Bickle et al., 2018) show lower fractions of carbonate weathering and sulfuric acid weathering, consistent with previous work showing that silicate weathering occurs

predominantly in the lowland hills and Himalayan flood-plain (Galy and France-Lanord, 1999; West et al., 2002; Lupker et al., 2012; Bickle et al., 2018; Bhatt et al., 2018).

5. CONCLUSIONS

Here we report the major ion concentrations and $\delta^{34}S_{SO4}$ of water samples collected monthly or bimonthly during 2011 from 16 sites along the Langtang-Trisuli-Narayani River system in the Nepal Himalaya. We evaluate the role of lithology and seasonality in the supply and $^{34}S/^{32}S$ isotope ratio of river SO_4^{2-} and account for the alkalinity flux from FeS_2 oxidation when evaluating the effect of Himalayan weathering on atmospheric pCO_2 over geologic time. Monte Carlo inversion modeling finds that, except for two samples, FeS_2 oxidation sources between 62% and 101% of dissolved SO_4^{2-} in our samples. We find that $\delta^{34}S_{SO4}$ principally reflects lithological $\delta^{34}S$ and is relatively constant at a given location throughout the sampled year. We recover spatial gradients in the magnitude of FeS_2 oxidation linked with weathering regime, as well as seasonal changes attributable to shifts in the relative importance of shallow and deep flow paths. Our results indicate that sulfide oxidation in the Narayani River catchment may fully counteract the CO_2 drawdown associated with silicate weathering on timescales longer than carbonate compensation (5–10 kyr) but shorter than the marine residence time of SO_4^{2-} (approximately10 Myr).

DATA AVAILABILITY

The measurements of $\delta^{34}S_{SO4}$ and dissolved major ion concentrations described in this article are available as supplementary material.

Declaration of Competing Interest

The authors declare that they have no known competing financial interests or personal relationships that could have appeared to influence the work reported in this paper.

APPENDIX. SUPPLEMENTARY MATERIAL

Supplementary data to this article can be found online at https://doi.org/10.1016/j.gca.2020.11.009.

REFERENCES

Andermann C., Bonnet S. and Gloaguen R. (2011) Evaluation of precipitation data sets along the Himalayan front. *Geochem. Geophys. Geosyst.* **12**(7).

Andermann C., Longuevergne L., Bonnet S., Crave A., Davy P. and Gloaguen R. (2012) Impact of transient groundwater storage on the discharge of Himalayan rivers. *Nat. Geosci.* **5**(2), 127.

Anderson S., Drever J. I. and Humphrey N. F. (1997) Chemical weathering in glacial environments. *Geology* **25**(5), 399–402.

Anderson S. P., Drever J. I., Frost C. D. and Holden P. (2000) Chemical weathering in the foreland of a retreating glacier. *Geochim. Cosmochim. Acta* **64**(7), 1173–1189.

Archer D., Kheshgi H. and Maier-Reimer E. (1997) Multiple timescales for neutralization of fossil fuel CO_2. *Geophys. Res. Lett.* **24**(4), 405–408.

Archer D., Winguth A., Lea D. and Mahowald N. (2000) What caused the glacial/interglacial atmospheric pCO_2 cycles? *Rev. Geophys.* **38**(2), 159–189.

Balci N., Shanks, III, W. C., Mayer B. and Mandernack K. W. (2007) Oxygen and sulfur isotope systematics of sulfate produced by bacterial and abiotic oxidation of pyrite. *Geochim. Cosmochim. Acta* **71**(15), 3796–3811.

Balestrini R., Polesello S. and Sacchi E. (2014) Chemistry and isotopic composition of precipitation and surface waters in Khumbu valley (Nepal Himalaya): N dynamics of high elevation basins. *Sci. Total Environ.* **485**, 681–692.

Beck R. A., Burbank D. W., Sercombe W. J., Riley G. W., Barndt J. K., Berry J. R. and Cheema A. (1995) Stratigraphic evidence for an early collision between northwest India and Asia. *Nature* **373**(6509), 55.

Becker J. A., Bickle M. J., Galy A. and Holland T. J. (2008) Himalayan metamorphic CO_2 fluxes: Quantitative constraints from hydrothermal springs. *Earth Planet. Sci. Lett.* **265**(3–4), 616–629.

Berner R. A. (1971) Worldwide sulfur pollution of rivers. *J. Geophys. Res.* **76**(27), 6597–6600.

Berner R. A. and Caldeira K. (1997) The need for mass balance and feedback in the geochemical carbon cycle. *Geology* **25**(10), 955–956.

Bhatt M. P., Masuzawa T., Yamamoto M., Sakai A. and Fujita K. (2000) Seasonal changes in dissolved chemical composition and flux of meltwater draining from Lirung Glacier in the Nepal Himalayas. *IAHS Publ.* **264**, 277–288.

Bhatt M. P., Masuzawa T., Yamamoto M. and Gardner K. H. (2009) Spatial variations in chemical compositions along Langtang-Narayani river system in central Nepal. *Environ. Geol.* **57**(3), 557–569.

Bhatt M. P., Hartmann J. and Acevedo M. F. (2018) Seasonal variations of biogeochemical matter export along the Langtang-Narayani river system in central Himalaya. *Geochim. Cosmochim. Acta* **238**, 208–234.

Bhattarai D. R. (1980) Some geothermal springs of Nepal. *Tectonophysics* **62**(1–2), 7–11.

Bickle M. J. (1996) Metamorphic decarbonation, silicate weathering and the long-term carbon cycle. *Terra Nova* **8**(3), 270–276.

Bickle M. J., Chapman H. J., Bunbury J., Harris N. B., Fairchild I. J., Ahmad T. and Pomiès C. (2005) Relative contributions of silicate and carbonate rocks to riverine Sr fluxes in the

headwaters of the Ganges. *Geochim. Cosmochim. Acta* **69**(9), 2221–2240.

Bickle M. J., Tipper E. D., Galy A., Chapman H. and Harris N. (2015) On discrimination between carbonate and silicate inputs to Himalayan rivers. *Am. J. Sci.* **315**(2), 120–166.

Bickle M. J., Chapman H. J., Tipper E., Galy A., Christina L. and Ahmad T. (2018) Chemical weathering outputs from the flood plain of the Ganga. *Geochim. Cosmochim. Acta* **225**, 146–175.

Blum J. D., Gazis C. A., Jacobson A. D. and Chamberlain P. (1998) Carbonate versus silicate weathering in the Raikhot watershed within the High Himalayan Crystalline Series. *Geology* **26**(5), 411–414.

Bluth G. J. and Kump L. R. (1994) Lithologic and climatologic controls of river chemistry. *Geochim. Cosmochim. Acta* **58**(10), 2341–2359.

Bordet P., Colchen M., Krummenacher D., Lefort P., Mouterde R. and Remy M. (1971) *Recherches Geologiques dans l'Himalaya du Nepal region de la Thakkhola*. Editions du centre national de la recherche scientifique.

Brantley S. L. and Lebedeva M. (2011) Learning to read the chemistry of regolith to understand the critical zone. *Annu. Rev. Earth Planet. Sci.* **39**, 387–416.

Brantley S. L., Holleran M. E., Jin L. and Bazilevskaya E. (2013) Probing deep weathering in the Shale Hills Critical Zone Observatory, Pennsylvania (USA): the hypothesis of nested chemical reaction fronts in the subsurface. *Earth Surf. Proc. Land.* **38**(11), 1280–1298.

Burke A., Present T. M., Paris G., Rae E. C., Sandilands B. H., Gaillardet J. and Voss B. M. (2018) Sulfur isotopes in rivers: Insights into global weathering budgets, pyrite oxidation, and the modern sulfur cycle. *Earth Planet. Sci. Lett.* **496**, 168–177.

Caldeira K. (1992) Enhanced Cenozoic chemical weathering and the subduction of pelagic carbonate. *Nature* **357**(6379), 578.

Calmels D., Gaillardet J., Brenot A. and France-Lanord C. (2007) Sustained sulfide oxidation by physical erosion processes in the Mackenzie River basin: Climatic perspectives. *Geology* **35**(11), 1003–1006.

Chakrapani G. J. and Veizer J. (2006) Source of dissolved sulphate in the Alakananda-Bhagirathi rivers in the Himalayas. *Curr. Sci.* **90**(4), 500–503.

Claypool G. E., Holser W. T., Kaplan I. R., Sakai H. and Zak I. (1980) The age curves of sulfur and oxygen isotopes in marine sulfate and their mutual interpretation. *Chem. Geol.* **28**, 199–260.

Collins R. and Jenkins A. (1996) The impact of agricultural land use on stream chemistry in the Middle Hills of the Himalayas, Nepal. *J. Hydrol.* **185**(1–4), 71–86.

Dalai T. K., Krishnaswami S. and Sarin M. M. (2002) Major ion chemistry in the headwaters of the Yamuna river system: Chemical weathering, its temperature dependence and CO_2 consumption in the Himalaya. *Geochim. Cosmochim. Acta* **66**(19), 3397–3416.

Dessert C., Dupré B., Gaillardet J., François L. M. and Allegre C. J. (2003) Basalt weathering laws and the impact of basalt weathering on the global carbon cycle. *Chem. Geol.* **202**(3–4), 257–273.

Dhital M. R. (2015) *Geology of the Nepal Himalaya: Regional Perspective of the Classic Collided Orogen*. Springer.

Edmond J. M. (1992) Himalayan tectonics, weathering processes, and the strontium isotope record in marine limestones. *Science* **258**(5088), 1594–1597.

Elderfield H. (1986) Strontium isotope stratigraphy. *Palaeogeogr. Palaeoclimatol. Palaeoecol.* **57**(1), 71–90.

Emberson R., Galy A. and Hovius N. (2017) Combined effect of carbonate and biotite dissolution in landslides biases silicate weathering proxies. *Geochim. Cosmochim. Acta* **213**, 418–434.

English N. B., Quade J., DeCelles P. G. and Garzione C. N. (2000) Geologic control of Sr and major element chemistry in Himalayan Rivers, Nepal. *Geochim. Cosmochim. Acta* **64**(15), 2549–2566.

Evans M. J., Derry L. A., Anderson S. P. and France-Lanord C. (2001) Hydrothermal source of radiogenic Sr to Himalayan rivers. *Geology* **29**(9), 803–806.

Evans M. J., Derry L. A. and France-Lanord C. (2004) Geothermal fluxes of alkalinity in the Narayani river system of central Nepal. *Geochem. Geophys. Geosyst.* **5**(8).

Evans M. J., Derry L. A. and France-Lanord C. (2008) Degassing of metamorphic carbon dioxide from the Nepal Himalaya. *Geochem. Geophys. Geosyst.* **9**(4).

Fort M. (1996) Late Cenozoic environmental changes and uplift on the northern side of the central Himalaya: a reappraisal from field data. *Palaeogeogr. Palaeoclimatol. Palaeoecol.* **120**(1–2), 123–145.

France-Lanord C. and Derry L. A. (1997) Organic carbon burial forcing of the carbon cycle from Himalayan erosion. *Nature* **390**(6655), 65.

François L. M. and Walker J. C. (1992) Modelling the Phanerozoic carbon cycle and climate: constraints from the $^{87}Sr/^{86}Sr$ isotopic ratio of seawater. *Am. J. Sci* **292**(2), 81–135.

Gabet E. J., Burbank D. W., Pratt-Sitaula B., Putkonen J. and Bookhagen B. (2008) Modern erosion rates in the High Himalayas of Nepal. *Earth Planet. Sci. Lett.* **267**(3–4), 482–494.

Gaillardet J., Dupré B., Louvat P. and Allegre C. J. (1999) Global silicate weathering and CO_2 consumption rates deduced from the chemistry of large rivers. *Chem. Geol.* **159**(1–4), 3–30.

Galy A. and France-Lanord C. (1999) Weathering processes in the Ganges-Brahmaputra basin and the riverine alkalinity budget. *Chem. Geol.* **159**(1–4), 31–60.

Galy V., France-Lanord C., Beyssac O., Faure P., Kudrass H. and Palhol F. (2007) Efficient organic carbon burial in the Bengal fan sustained by the Himalayan erosional system. *Nature* **450**(7168), 407–410.

Girault F., Bollinger L., Bhattarai M., Koirala B. P., France-Lanord C., Rajaure S. and Perrier F. (2014) Large-scale organization of carbon dioxide discharge in the Nepal Himalayas. *Geophys. Res. Lett.* **41**(18), 6358–6366.

Glover D. M., Jenkins W. J. and Doney S. C. (2011) *Modeling Methods for Marine Science*. Cambridge University Press.

Godsey S. E., Kirchner J. W. and Clow D. W. (2009) Concentration–discharge relationships reflect chemostatic characteristics of US catchments. *Hydrol. Process.* **23**(13), 1844–1864.

Godsey S. E., Hartmann J. and Kirchner J. W. (2019) Catchment chemostasis revisited: Water quality responds differently to variations in weather and climate. *Hydrol. Process.* **33**(24), 3056–3069.

Gu X., Rempe D. M., Dietrich W. E., West A. J., Lin T. C., Jin L. and Brantley S. L. (2020) Chemical reactions, porosity, and microfracturing in shale during weathering: The effect of erosion rate. *Geochim. Cosmochim. Acta* **269**, 63–100.

Handa B. K. (1968) The chemical composition of rain water in some parts of North India. *Indian J. Meteorol. Geophys.* **19**, 175–180.

Harris N., Bickle M., Chapman H., Fairchild I. and Bunbury J. (1998) The significance of Himalayan rivers for silicate weathering rates: evidence from the Bhote Kosi tributary. *Chem. Geol.* **144**(3–4), 205–220.

Hemingway J. D., Olson H., Turchyn A. V., Tipper E. T., Bickle M. J. and Johnston D. T. (2020) Triple oxygen isotope insight into terrestrial pyrite oxidation. *Proceedings of the National Academy of Sciences* **117**(14), 7650–7657.

Hilton R. G., Gaillardet J., Calmels D. and Birck J. L. (2014) Geological respiration of a mountain belt revealed by the trace element rhenium. *Earth Planet. Sci. Lett.* **403**, 27–36.

Hilton R. G. and West A. J. (2020) Mountains, erosion and the carbon cycle. *Nature Rev. Earth Environ.* **1**(6), 284–299.

Horan K., Hilton R. G., Dellinger M., Tipper E., Galy V., Calmels D. and Burton K. W. (2019) Carbon dioxide emissions by rock organic carbon oxidation and the net geochemical carbon budget of the Mackenzie River Basin. *American Journal of Science* **319**(6), 473–499.

Horita J., Zimmermann H. and Holland H. D. (2002) Chemical evolution of seawater during the Phanerozoic: Implications from the record of marine evaporites. *Geochim. Cosmochim. Acta* **66**(21), 3733–3756.

Hren M. T., Chamberlain C. P., Hilley G. E., Blisniuk P. M. and Bookhagen B. (2007) Major ion chemistry of the Yarlung Tsangpo-Brahmaputra river: chemical weathering, erosion, and CO_2 consumption in the southern Tibetan plateau and eastern syntaxis of the Himalaya. *Geochim. Cosmochim. Acta* **71**(12), 2907–2935.

Huh Y., Tsoi M. Y., Zaitsev A. and Edmond J. M. (1998) The fluvial geochemistry of the rivers of Eastern Siberia: I. Tributaries of the Lena River draining the sedimentary platform of the Siberian Craton. *Geochim. Cosmochim. Acta* **62**(10), 1657–1676.

Ibarra D. E., Caves J. K., Moon S., Thomas D. L., Hartmann J., Chamberlain C. P. and Maher K. (2016) Differential weathering of basaltic and granitic catchments from concentration–discharge relationships. *Geochim. Cosmochim. Acta* **190**, 265–293.

Inger S. and Harris N. B. W. (1992) Tectonothermal evolution of the High Himalayan crystalline sequence, Langtang Valley, northern Nepal. *J. Metamorph. Geol.* **10**(3), 439–452.

Inger S. and Harris N. (1993) Geochemical constraints on leucogranite magmatism in the Langtang Valley, Nepal Himalaya. *J. Petrol.* **34**(2), 345–368.

Ivanov M. V., Grinenko V. A. and Rabinovich A. P. (1983) The sulphur cycle in continental reservoirs. *Global Biogeochem. Sulphur Cycle-Scope* **39**, 297–356.

Jacobson A. D., Blum J. D. and Walter L. M. (2002) Reconciling the elemental and Sr isotope composition of Himalayan weathering fluxes: insights from the carbonate geochemistry of stream waters. *Geochim. Cosmochim. Acta* **66**(19), 3417–3429.

John S. G. and Adkins J. F. (2010) Analysis of dissolved iron isotopes in seawater. *Mar. Chem.* **119**(1–4), 65–76.

Johnson J. E., Gerpheide A., Lamb M. P. and Fischer W. W. (2014) O_2 constraints from Paleoproterozoic detrital pyrite and uraninite. *Bulletin* **126**(5–6), 813–830.

Karim A. and Veizer J. (2000) Weathering processes in the Indus River Basin: implications from riverine carbon, sulfur, oxygen, and strontium isotopes. *Chem. Geol.* **170**(1–4), 153–177.

Kerrick D. M. and Caldeira K. (1999) Was the Himalayan orogen a climatically significant coupled source and sink for atmospheric CO_2 during the Cenozoic? *Earth Planet. Sci. Lett.* **173**(3), 195–203.

Krishnaswami S. and Singh S. K. (1998) Silicate and carbonate weathering in the drainage basins of the Ganga-Ghaghara-Indus head waters: Contributions to major ion and Sr isotope geochemistry. *Proc. Indian Acad. Sci.-Earth Planet. Sci.* **107**(4), 283–291.

Krishnaswami S., Singh S. K. and Dalai T. K. (1999) Silicate weathering in the Himalaya: Role in contributing to major ions and radiogenic Sr to the Bay of Bengal. In *Ocean Science, Trends and Future Directions, India* (ed. B. L. K. Somayajulu), pp. 23–51.

Kump L. R. and Arthur M. A. (1997) Global chemical erosion during the Cenozoic: Weatherability balances the budgets. In *Tectonic Uplift and Climate Change*. Springer, Boston, MA, pp. 399–426.

Lerman A., Wu L. and Mackenzie F. T. (2007) CO_2 and H_2SO_4 consumption in weathering and material transport to the ocean, and their role in the global carbon balance. *Mar. Chem.* **106**(1–2), 326–350.

Li G. and Elderfield H. (2013) Evolution of carbon cycle over the past 100 million years. *Geochim. Cosmochim. Acta* **103**, 11–25.

Lupker M., France-Lanord C., Galy V., Lavé J., Gaillardet J., Gajurel A. P. and Sinha R. (2012) Predominant floodplain over mountain weathering of Himalayan sediments (Ganga basin). *Geochim. Cosmochim. Acta* **84**, 410–432.

Macnamara J. and Thode H. G. (1950) Comparison of the isotopic constitution of terrestrial and meteoritic sulfur. *Phys. Rev.* **78**(3), 307.

Maher K. and Chamberlain C. P. (2014) Hydrologic regulation of chemical weathering and the geologic carbon cycle. *Science* **343**(6178), 1502–1504.

Millot R., Gaillardet J., Dupré B. and Allègre C. J. (2002) The global control of silicate weathering rates and the coupling with physical erosion: new insights from rivers of the Canadian Shield. *Earth Planet. Sci. Lett.* **196**(1–2), 83–98.

Myrow P. M., Hughes N. C., Derry L. A., McKenzie N. R., Jiang G., Webb A. A. G. and Singh B. P. (2015) Neogene marine isotopic evolution and the erosion of Lesser Himalayan strata: Implications for Cenozoic tectonic history. *Earth Planet. Sci. Lett.* **417**, 142–150.

Négrel P., Allègre C. J., Dupré B. and Lewin E. (1993) Erosion sources determined by inversion of major and trace element ratios and strontium isotopic ratios in river water: the Congo Basin case. *Earth Planet. Sci. Lett.* **120**(1–2), 59–76.

Otto-Bliesner B. L. (1995) Continental drift, runoff, and weathering feedbacks: Implications from climate model experiments. *J. Geophys. Res.: Atmos.* **100**(D6), 11537–11548.

Pant R. R., Zhang F., Rehman F. U., Wang G., Ye M., Zeng C. and Tang H. (2018) Spatiotemporal variations of hydrogeochemistry and its controlling factors in the Gandaki River Basin, Central Himalaya Nepal. *Sci. Total Environ.* **622**, 770–782.

Panthi J., Dahal P., Shrestha M., Aryal S., Krakauer N., Pradhanang S. and Karki R. (2015) Spatial and temporal variability of rainfall in the Gandaki River Basin of Nepal Himalaya. *Climate* **3**(1), 210–226.

Paris G., Sessions A. L., Subhas A. V. and Adkins J. F. (2013) MC-ICP-MS measurement of $\delta^{34}S$ and $\Delta^{33}S$ in small amounts of dissolved sulfate. *Chem. Geol.* **345**, 50–61.

Pierson-Wickmann A. C., Reisberg L. and France-Lanord C. (2000) The Os isotopic composition of Himalayan river bedloads and bedrocks: importance of black shales. *Earth Planet. Sci. Lett.* **176**(2), 203–218.

Quade J., English N. and DeCelles P. G. (2003) Silicate versus carbonate weathering in the Himalaya: a comparison of the Arun and Seti River watersheds. *Chem. Geol.* **202**(3–4), 275–296.

Quay P. D., Wilbur D. O., Richey J. E., Devol A. H., Benner R. and Forsberg B. R. (1995) The $^{18}O:^{16}O$ of dissolved oxygen in rivers and lakes in the Amazon Basin: determining the ratio of respiration to photosynthesis rates in freshwaters. *Limnol. Oceanogr.* **40**(4), 718–729.

Rabinovich A. L. and Grinenko V. A. (1979) Sulfate sulfur isotope ratios for USSR River water. *Geochem. Int.* **16**, 68–79.

Raymo M. E., Ruddiman W. F. and Froelich P. N. (1988) Influence of late Cenozoic mountain building on ocean geochemical cycles. *Geology* **16**(7), 649–653.

Raymo M. E. and Ruddiman W. F. (1992) Tectonic forcing of late Cenozoic climate. *Nature* **359**(6391), 117.

Raymo M. (1994) The Himalayas, organic carbon burial, and climate in the Miocene. *Paleoceanogr. Paleoclimatol.* **9**(3), 399–404.

Raymond P. A., Hartmann J., Lauerwald R., Sobek S., McDonald C., Hoover M. and Kortelainen P. (2013) Global carbon dioxide emissions from inland waters. *Nature* **503**(7476), 355–359.

Rennie V. C., Paris G., Sessions A. L., Abramovich S., Turchyn A. V. and Adkins J. F. (2018) Cenozoic record of δ^{34}S in foraminiferal calcite implies an early Eocene shift to deep-ocean sulfide burial. *Nat. Geosci.* **11**(10), 761.

Riebe C. S., Kirchner J. W., Granger D. E. and Finkel R. C. (2001) Strong tectonic and weak climatic control of long-term chemical weathering rates. *Geology* **29**(6), 511–514.

Roback K., Clark M. K., West A. J., Zekkos D., Li G., Gallen S. F. and Godt J. W. (2018) The size, distribution, and mobility of landslides caused by the 2015 Mw7. 8 Gorkha earthquake, Nepal. *Geomorphology* **301**, 121–138.

Sarin M. M. and Krishnaswami S. (1984) Major ion chemistry of the Ganga-Brahmaputra river systems, India. *Nature* **312** (5994), 538.

Sarin M. M., Krishnaswami S., Dilli K., Somayajulu B. L. K. and Moore W. S. (1989) Major ion chemistry of the Ganga-Brahmaputra river system: Weathering processes and fluxes to the Bay of Bengal. *Geochim. Cosmochim. Acta* **53**(5), 997–1009.

Sarmiento J. L. and Gruber N. (2006) *Ocean Biogeochemical Dynamics*. Princeton University Press.

Sequeira R. and Kelkar D. (1978) Geochemical implications of summer monsoonal rainwater composition over India. *J. Appl. Meteorol.* **17**(9), 1390–1396.

Shrestha A. B., Wake C. P., Dibb J. E. and Whitlow S. I. (2002) Aerosol and precipitation chemistry at a remote Himalayan site in Nepal. *Aerosol Sci. Technol.* **36**(4), 441–456.

Sim M. S., Bosak T. and Ono S. (2011) Large sulfur isotope fractionation does not require disproportionation. *Science* **333** (6038), 74–77.

Singh S. P. and Singh B. P. (2010) Geothermal evolution of the evaporite-bearing sequences of the Lesser Himalaya, India. *Int. J. Earth Sci.* **99**(1), 101–108.

Spence J. and Telmer K. (2005) The role of sulfur in chemical weathering and atmospheric CO_2 fluxes: evidence from major ions, $\delta^{13}C_{DIC}$, and $\delta^{34}S_{SO4}$ in rivers of the Canadian Cordillera. *Geochim. Cosmochim. Acta* **69**(23), 5441–5458.

Stallard R. F. and Edmond J. M. (1983) Geochemistry of the Amazon: 2. The influence of geology and weathering environment on the dissolved load. *J. Geophys. Res. Oceans* **88**(C14), 9671–9688.

Striegl R. G., Dornblaser M. M., McDonald C. P., Rover J. R. and Stets E. G. (2012) Carbon dioxide and methane emissions from the Yukon River system. *Global Biogeochem. Cycles* **26**(4).

Sundquist E. T. (1991) Steady-and non-steady-state carbonate-silicate controls on atmospheric CO_2. *Quat. Sci. Rev.* **10**(2–3), 283–296.

Tipper E. T., Bickle M. J., Galy A., West A. J., Pomiès C. and Chapman H. J. (2006) The short term climatic sensitivity of carbonate and silicate weathering fluxes: insight from seasonal variations in river chemistry. *Geochim. Cosmochim. Acta* **70**(11), 2737–2754.

Tipper E. T., Galy A. and Bickle M. J. (2008) Calcium and magnesium isotope systematics in rivers draining the Himalaya-Tibetan-Plateau region: Lithological or fractionation control? *Geochim. Cosmochim. Acta* **72**(4), 1057–1075.

Thode H. G., Kleerekoper H. and McElcheran D. (1951) Isotope fractionation in the bacterial reduction of sulphate. *Research* **4** (12), 581.

Thode H. G. (1991) Sulphur isotopes in nature and the environment: an overview. *Stable Isotopes: Natural and Anthropogenic Sulphur in the Environment* **43**, 1–26.

Torres M. A., West A. J. and Li G. (2014) Sulphide oxidation and carbonate dissolution as a source of CO_2 over geological timescales. *Nature* **507**(7492), 346.

Torres M. A., West A. J., Clark K. E., Paris G., Bouchez J., Ponton C. and Adkins J. F. (2016) The acid and alkalinity budgets of weathering in the Andes-Amazon system: Insights into the erosional control of global biogeochemical cycles. *Earth Planet. Sci. Lett.* **450**, 381–391.

Torres M. A., Moosdorf N., Hartmann J., Adkins J. F. and West A. J. (2017) Glacial weathering, sulfide oxidation, and global carbon cycle feedbacks. *Proc. Natl. Acad. Sci.* **114**(33), 8716–8721.

Tranter M. and Wadham J. L. (2014) Geochemical weathering in glacial and proglacial environments. In *Surface and Ground Water, Weathering and Soils* (eds. H. D. Holland and K. K. Turekian), Treatise on Geochemistry 2nd edition. Elsevier.

Tripathee L., Kang S., Huang J., Sharma C. M., Sillanpää M., Guo J. and Paudyal R. (2014) Concentrations of trace elements in wet deposition over the central Himalayas, Nepal. *Atmos. Environ.* **95**, 231–238.

Tshering L. D. and Bhandari A. N. (1973) *Geological Report on the Salt Occurrences of Mustang Area*. Ministry of Industry & Commerce, Nepal Geological Survey.

Turchyn A. V., Tipper E. T., Galy A., Lo J. K. and Bickle M. J. (2013) Isotope evidence for secondary sulfide precipitation along the Marsyandi River, Nepal, Himalayas. *Earth Planet. Sci. Lett.* **374**, 36–46.

Urey H. C. (1952) On the early chemical history of the earth and the origin of life. *Proc. Natl. Acad. Sci. U. S. Am.* **38**(4), 351.

Valdiya K. S. (1980) *Geology of the Kumaun Lesser Himalayas*. Wadia Institute of the Himalayan Geology, Dehra Dun, India.

Veizer J. (1989) Strontium isotopes in seawater through time. *Annu. Rev. Earth Planet. Sci.* **17**(1), 141–167.

Walker J. C., Hays P. B. and Kasting J. F. (1981) A negative feedback mechanism for the long-term stabilization of Earth's surface temperature. *J. Geophys. Res. Oceans* **86**(C10), 9776–9782.

West A. J., Bickle M. J., Collins R. and Brasington J. (2002) Small-catchment perspective on Himalayan weathering fluxes. *Geology* **30**(4), 355–358.

West A. J., Galy A. and Bickle M. (2005) Tectonic and climatic controls on silicate weathering. *Earth Planet. Sci. Lett.* **235**(1–2), 211–228.

West A. J. (2012) Thickness of the chemical weathering zone and implications for erosional and climatic drivers of weathering and for carbon-cycle feedbacks. *Geology* **40**(9), 811–814.

White A. F. and Blum A. E. (1995) Effects of climate on chemical weathering in watersheds. *Geochim. Cosmochim. Acta* **59**(9), 1729–1747.

Winnick M. J., Carroll R. W., Williams K. H., Maxwell R. M., Dong W. and Maher K. (2017) Snowmelt controls on concentration-discharge relationships and the balance of oxidative and acid-base weathering fluxes in an alpine catchment, East River, Colorado. *Water Resour. Res.* **53**(3), 2507–2523.

Wolff-Boenisch D., Gabet E. J., Burbank D. W., Langner H. and Putkonen J. (2009) Spatial variations in chemical weathering and CO_2 consumption in Nepalese High Himalayan catchments during the monsoon season. *Geochim. Cosmochim. Acta* **73**(11), 3148–3170.

Zachos J., Pagani M., Sloan L., Thomas E. and Billups K. (2001) Trends, rhythms, and aberrations in global climate 65 Ma to present. *Science* **292**(5517), 686–693.

Zeebe, R.E., Wolf-Gladrow, D., 2001. CO_2 in Seawater: Equilibrium, Kinetics, Isotopes (No. 65). Gulf Professional Publishing.

Associate editor: Martin Novak